Draft version 00: proposal for the PAC 46, Timelike Compton Scattering off a transversely polarized proton

May 16, 2018

Abstract

We propose to measure Timelike Compton Scattering (TCS) off the proton using a transversely polarized target. TCS reaction corresponds to the scattering of a real photon off a quark, followed by the emission of a high virtuality photon, which decays into a lepton pair. TCS can be parametrized by Generalized Parton Distributions (GPDs), containing information about the transverse spatial distribution of quarks and their longitudinal momentum inside the proton. Thanks to a transversely polarized proton target and a real circularly polarized photon beam, we can access 4 independent observables sensitive to GPDs, in particular the GPD E. This experiment will also allow for demonstrating GPDs universality by comparison of GPDs extracted independently from other reactions, such as Deeply Virtual Compton Scattering.

1 Introduction

The Timelike Compton Scattering (TCS) process corresponds to the exclusive photoproduction of a lepton pair with exchange of a high virtuality photon. A real photon is scattered off a quark of the nucleon, and a high virtuality photon is emitted, then decays into a lepton pair ($\gamma N \hookrightarrow \gamma^* N' \rightarrow e^+e^-N'$, Fig. 1). Typically, the photon virtuality $Q'^2 = +q'2 = (k - k')^2$ (where q', k, k' are the 4-momenta of the virtual photon, the electron and the positron respectively), is greater than ~ 1 GeV^2 to allow for factorization of the TCS amplitude between a hard part, calculable from perturbative QED (upper part of the diagram 1) and a soft QCD non perturbative part (lower part of the diagram 1). TCS is sensitive to the transverse spatial distribution of partons in the nucleon and the correlation with their longitudinal momentum. It can be parametrized by Generalized Parton Distributions (GPDs), which have been introduced in [1, 2, 3]. Assuming massless quarks, at QCD leading order and leading twist, we can parametrize TCS with 4 helicity conserving quark GPDs: H, E, $\tilde{\mathrm{H}}$, $\tilde{\mathrm{E}}$. They correspond to 4 independent helicity-spin transitions between the initial quark-proton system and the final one, and are the Fourier transform of the QCD matrix element of the soft part of the TCS amplitude. Given the kinematic domain accessible at JLab, we neglect GPDs of gluons. At leading order, the GPDs depend on 3 independent variables: x is the longitudinal momentum fraction of the nucleon momentum carried by the quark, ξ is proportionnal to the longitudinal momentum transfer to the quark, and t is the square 4-momentum transfer to the nucleon, i.e. t=(p-p')^2, where p and p' are the 4-momenta of the incoming and outgoing nucleon respectively. We refer to the reviews [4, 5, 3, 6] for details about GPD formalism and physics interests.

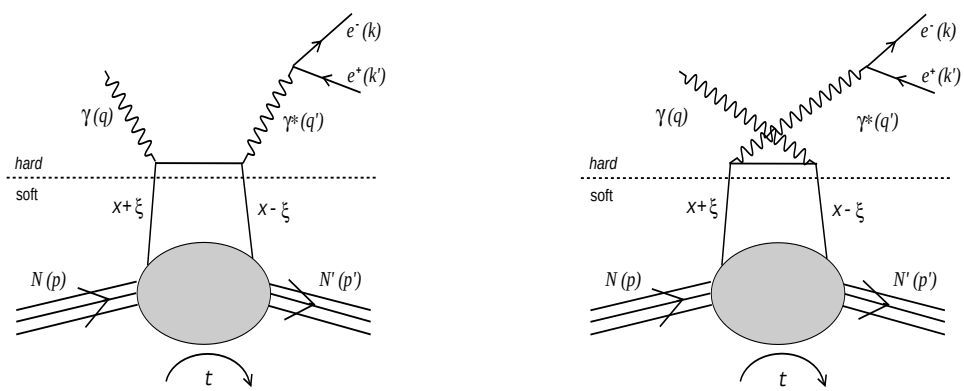

Figure 1: TCS leading order and leading twist handbag diagrams.

TCS interfers with a Bethe-Heitler like process (BH), where the incoming real photon splits into a lepton pair in the nucleon field (Fig. 2). BH depends on the nucleon Form Factors (FFs) and is not sensitive to GPDs. Since TCS and BH leads to the same final state, experimental measurements of the hard exclusive lepton pair photoproduction reaction contain the two processes and their interference, and cannot be measured separately. As it will be discussed later, the BH amplitude is always largely dominant compared to the TCS one at JLab kinematics. However, the interference between BH and TCS is enhancing TCS, which would have a rather small cross section otherwise. Several spin dependent observables (from polarized beam and/or target) allow

for accessing directly or indirectly the TCS+BH interference term, and indeed information about GPDs, as discussed in [12, 13]. Measuring several independent observables allow for extracting the GPDs, as it will be shown later. We don't access directly GPDs, due to their x dependence is contained into integrals in the amplitudes, but rather we can access Compton Form Factors (CFFs), which are complex functions of GPDs depending on ξ and t (at LO). In our notations, we associate 2 CFFs to each GPD, corresponding to the imaginary and the real part of the CFFs, such as the CFF $\Im\mathcal{H}$ and $\Re\mathcal{H}$ are functions of the GPD H.

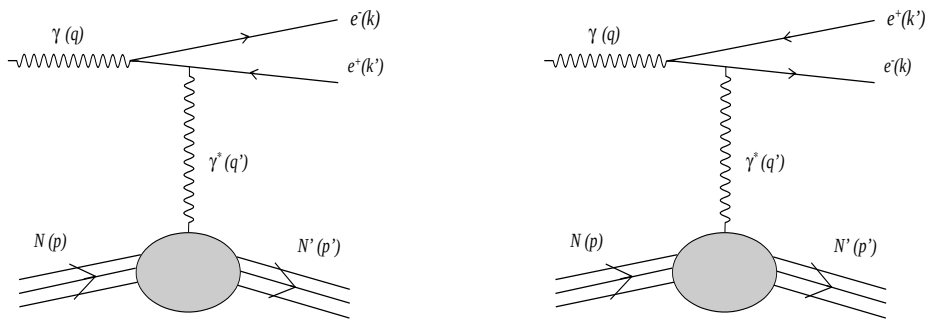

Figure 2: Bethe-Heitler process interfering with TCS, leading order and leading twist diagrams.

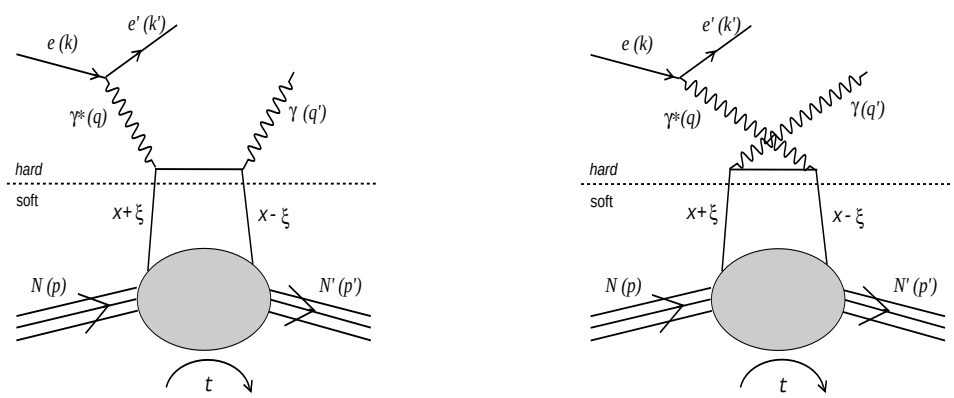

Figure 3: DVCS leading order and leading twist handbag diagrams.

An analogy can be made between TCS and Deeply Virtual Compton Scattering (DVCS = $eN \hookrightarrow \gamma^* N \rightarrow e' N' \gamma$ - Fig. 3), which corresponds to the scattering of a high virtuality photon, coming from a lepton beam, off a quark of the nucleon. DVCS has been intensively studied over the past 15 years, and measurements of DVCS observables already lead to DVCS CFFs and GPDs measurements, constraining GPD models [6]. However, the real part of DVCS CFFs is poorly constrained by existing measurements. While different models are in good agreement for imaginary part of CFFs, predictions differ on the real part. In addition, the GPD E is poorly constrained and there is a real need of independent measurements sensitive to it. GPD E contain information about the

quarks angular momenta and their distribution in a transversely polarized nucleon. Ji sum rule [2] relates GPDs H and E to the nucleon orbital momentum, and shows that it is possible to study the quark and nucleon spin correlations thanks to GPDs in addition to inclusive and semi-inclusive measurements [**?**]. Ji sum rule for quark GPDs reads

$$J^q(t=0) = \frac{1}{2}\int dx\, x\,[H^q(x,\xi,t=0) + E^q(x,\xi,t=0)] = \frac{1}{2}\Delta\Sigma + L_q \quad (\forall\xi), \tag{1}$$

where L_q is the quark angular momentum and $\Delta\Sigma$ is the fraction of the nucleon spin carried by the quarks ($\Delta\Sigma \approx 0.3$). Indeed, there is a strong interest in measuring GPD E to understand the quark orbital momentum contribution to the proton spin, i.e. to understand how the nucleon spin is distributed within its constituants.

As demonstrated in [5], DVCS and TCS amplitudes are complex conjugate at leading order. Both processes access the same GPDs at the same kinematic points (ξ, t), and their CFFs are complex conjugates. Demonstrating the universality of QCD structure functions such as GPDs is a milestone. Comparing GPDs extracted from DVCS (spacelike process) to GPDs extracted from TCS (timelike process) is therefore one of the most important result we can obtain from our TCS experiment in addition to other independent DVCS measurement. We will therefore demonstrate the feasibility of extracting CFFs from TCS observables, at a level comparable with DVCS. Furthermore, as the only soft part involved in the DVCS and TCS processes corresponds to the GPDs, these two processes can be seen as the cleanest one to access GPDs without additional unknown.

Assuming, or after demonstrating, that GPDs are universal, constraining GPD E from TCS measurements will be complementary to the existing and planned measurements of DVCS in the JLab 12 GeV program. Indeed, under the assumption of GPD universality and neglecting higher twist and higher order effects in DVCS and TCS, it is possible to complementarly constrain GPDs from DVCS and from TCS measurement as we will demonstrate. TCS observables, particularly the transversely polarized target cross sections, bring new independent information and allow to extract all proton CFFs simultenaously in a multi-parameters, multi-observables CFFs fitting approach.

In the following, we will present the TCS formalism and the observables we intend to measure. We will discuss the impact of the measurements and the projection of experimental uncertainties. We propose an experimental setup, which use an untagged bremsstrahlung photon beam from the Compact Photon Source [32], the UVa transvesally polarized ammonia NH_3 target [28, 29], detectors for the recoil proton detection and a pair of electromagnetic calorimeters, similar than the one of the Neutral Particle Spectrometer project [].

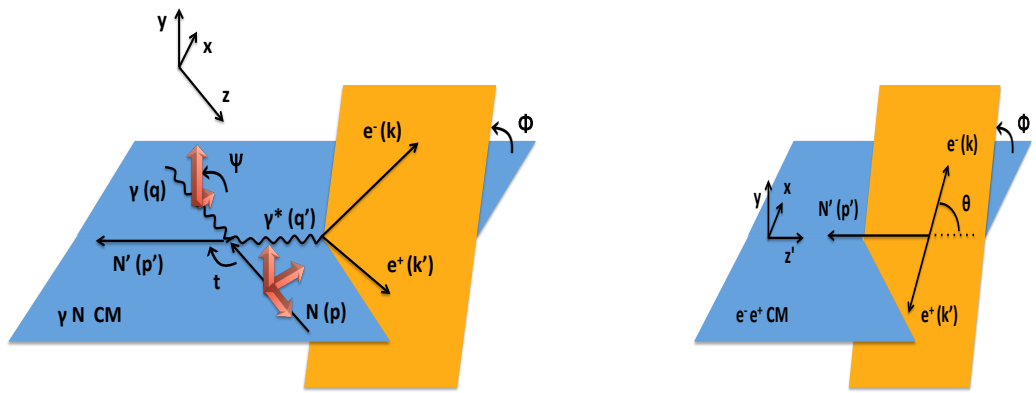

Figure 4: Scheme of the TCS reaction in the nucleon-photon center of mass frame (left panel) and in the final photon rest frame (right panel). The momentum of incoming and outgoing nucleon, real and virtual photon, electron and positron are indicated by letters p, p′, q, q′, k and k′, respectively. Left panel: we indicated the angle ϕ_{CM} between the lepton decay plane and the reaction plane. We also indicated by red arrows the possible orientations of beam and target spin. Right panel: ϕ_{CM} angle is conserved in the boost from γN to γ^* C.M. frames. θ_{CM} is the angle between the lepton direction and the boost axis, defined by the γ^* direction in the γN C.M. frame.

2 Physics case

2.1 TCS formalism

The unpolarized TCS+BH cross section depends on five independent variables. We express it either as a function of the beam energy (E_γ) either as a function of the longitudinal momentum transfer $\xi = \frac{Q'^2}{2s-Q'^2}$, where s=(p+q)^2 is the squared C.M. energy of the reaction. The definition of ξ is valid at the asymptotic limit (t/Q′^{2} $\rightarrow 0$) (we refer to [12] for details). We also express the cross section as a function of the momentum transfer squared t, the virtuality of the final photon Q′^{2}, and the polar and azimuthal angles of the electron in the C.M. frame of the lepton pair versus the reaction plane (the γ, γ^* plane). These angles are represented on Fig. 4. Left panel is a scheme of the reaction in the C.M. frame of the incoming photon and proton. The variables and angles represented in the scheme are explicit in the legend. Fig. 4 (right panel) shows the angles in the virtual photon C.M. frame. The longitudinal axis for the boost between the two frames is used as reference for the final electron polar angle.

At fixed beam energy (or fix ξ), averaging over the beam, the initial and the final nucleon helicities, we express the 4-differential BH+TCS unpolarized cross section as

$$\frac{d^4\sigma}{dQ'^2 dt d\Omega}(\gamma p \rightarrow p' e^+ e^-) = \frac{1}{2\pi^4}\frac{1}{64}\frac{1}{(2m_N E_\gamma)^2} \mid T^{BH} + T^{TCS} \mid^2,$$

where the $\mid T^{BH} + T^{TCS} \mid^2$ term corresponds to the BH and TCS amplitudes. and m_N is the nucleon mass. The polarized nucleon cross sections also depends on the angles between the nucleon spin direction and the reaction plane, ϕ_S and θ_S We display in Fig. 4 the particular cases of spin along the z-axis ($\theta_S = 0°$), along the x-axis ($\theta_S = 90°$ and $\phi_S = 0°$) and along the y-axis ($\theta_S = 90°$ and $\phi_S = 90°$).

The TCS amplitude reads

$$T^{TCS} = -\frac{e^3}{q'^2}\, \bar{u}(k)\, \gamma^\nu\, v(k')\, \epsilon^\mu(q)\, H^{TCS}_{\mu\nu}, \tag{2}$$

with, at the asymptotic limit,

$$\begin{aligned} & H^{TCS}_{\mu\nu} \\ & = \frac{1}{2}\,(-g_{\mu\nu})_\perp \int_{-1}^{1} dx\, \left(\frac{1}{x-\xi-i\epsilon} + \frac{1}{x+\xi+i\epsilon}\right) \\ & .\left(H(x,\xi,t)\bar{u}(p')\not{n}u(p) + E(x,\xi,t)\bar{u}(p')i\sigma^{\alpha\beta}n_\alpha\frac{\Delta_\beta}{2m}\, u(p)\right) \\ & -\frac{i}{2}(\epsilon_{\nu\mu})_\perp \int_{-1}^{1} dx\, \left(\frac{1}{x-\xi-i\epsilon} - \frac{1}{x+\xi+i\epsilon}\right) \\ & .\left(\tilde{H}(x,\xi,t)\bar{u}(p')\not{n}\gamma_5\, u(p) + \tilde{E}(x,\xi,t)\bar{u}(p')\gamma_5\frac{\Delta.n}{2m}\, u(p)\right), \end{aligned} \tag{3}$$

where we used the metric:

$$\begin{aligned} (-g_{\mu\nu})_\perp &= -g_{\mu\nu} + \tilde{p}_\mu n_\nu + \tilde{p}_\nu n_\mu\ , \\ (\epsilon_{\nu\mu})_\perp &= \epsilon_{\nu\mu\alpha\beta}\, n^\alpha\, \tilde{p}^\beta. \end{aligned} \tag{4}$$

The GPDs entering Eq. 3 are proton GPDs, i.e. they read, in terms of quark flavors:

$$H_{TCS}(x,\xi,t)\ =\ \frac{4}{9}H^{u/p}\ +\ \frac{1}{9}H^{d/p}\ +\ \frac{1}{9}H^{s/p}. \tag{5}$$

We use the decomposition into GPDs and notations from Ji [**?**], and the GPD parametrizations from VGG model [7, 8, 4, 9], which are summarized in Ref. [6] and based on the Radyushkin double-distribution ansatz for the (x,ξ)-dependence [10, 11, 1] and on the Reggeized ansatz for the t-distribution [4, 9].

The BH amplitude can be expressed as

$$T^{BH} = -\frac{e^3}{\Delta^2}\, \bar{N}\, \Gamma^\nu\, N\, \epsilon^\mu(q)\, \bar{u}(k)\, \left(\gamma_\mu\frac{\not{k}-\not{q}}{(k-q)^2}\gamma_\nu + \gamma_\nu\frac{\not{q}-\not{k}'}{(q-k')^2}\gamma_\mu\right)\, v(k'), \tag{6}$$

where the 4-vectors q, k, k′ respectively correspond to the photon, the electron and the positron. N corresponds to the nucleon spinor and Δ is the proton momentum transfer. The virtual photon-proton electromagnetic vertex matrix can be expressed as a function of Dirac (F_1) and Pauli (F_2) form factors

$$\Gamma^\nu = \gamma^\nu\, F_1(t) + \frac{i\sigma^{\nu\rho}\Delta_\rho}{2\, m_N}\, F_2(t), \tag{7}$$

The BH amplitude depends on the proton Dirac and Pauli form factors $F_1(t)$ and $F_2(t)$. We use the electric form factor parametrization from [18] and magnetic form factor parametrization from [19]. We refer for more details about the formalism used to [12].

2.2 Observables

2.2.1 Unpolarized cross section

Using a real circularly polarized photon beam and a transversely polarized target, there are 4 independent observables that can be accessed from the TCS+BH reaction. We display on Fig. 5 the TCS and BH unpolarized cross section as a function of ϕ for various θ angles. In the analysis, we will integrate the cross sections over θ in a range depending on the kinematics (this point will be discussed in section 4.2).

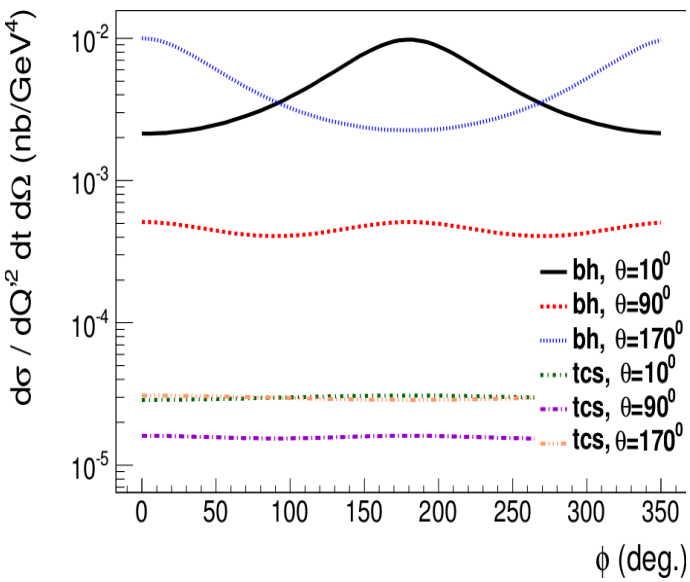

Figure 5: BH and TCS cross sections as a function of ϕ at Q'^2 = 7 GeV^2, -t=0.4 GeV^2, ξ=0.2, for $\theta_{CM} = 10°$, $\theta_{CM} = 170°$ and $\theta_{CM} = 90°$.

For polarization observables, we use the following notations:

- We use the notation for an asymmetry $A_{PP'}$, with two indices P and P'. The first index P refers to the polarization type of the beam: U for an unpolarized beam, $P = \odot$ and for a circularly polarized beam. The second index P' refers to the polarization of the target and can take the values U (unpolarized), x ($\phi_S = 0°$), y ($\phi_S = 90°$), or T for any generic value of ϕ_S.
- Similarly, we use the notation $\sigma_{PP'}$ for polarized cross sections and $\Delta\sigma_{PP'}$ for polarized cross section differences, defined as the difference of polarized cross sections $\sigma_{PP'}$, with spin vectors pointing in opposite directions.

2.2.2 Circularly polarized beam spin asymmetry

We define the circularly polarized beam spin asymmetry as

$$A_{\odot U} = \frac{\sigma^+ - \sigma^-}{\sigma^+ + \sigma^-}, \tag{8}$$

where $\sigma^\pm$ stand for the 4-fold differential cross sections $\frac{d\sigma}{dQ'^2\, dt\, d\phi\, d(cos\theta)}$ for the two photon circular polarization states (right and left polarized). We display in Fig. 6 (top panel) our results for $A_{\odot U}$

as a function of ϕ at $Q'^2 = 7$ GeV^2, $\xi = 0.2$, $-t = 0.4$ GeV^2 for θ integrated over $[45°, 135°]$. We observe that the BH doesn't produce any asymmetry. Any signal therefore reflects a contribution from TCS. This is due to the fact that this observable is sensitive to the imaginary part of the amplitude, and that the BH amplitude is purely real. Since the BH does not produce on its own an asymmetry, we show in [12] the integration over θ does not strongly reduce the signal, and that we obtain a relatively large (∼20%) sin(ϕ)-shape asymmetry. The result is displayed using different GPDs parametrizations for TCS. In Fig. **??**, we show for $\xi = 0.2$, $Q'^2 = 7$ GeV^2, $\phi = 90°$ and θ integrated over $[45°, 135°]$, the t-dependence of $A_{\odot U}$ and its sensitivity to different GPDs. We notice that the magnitude of $A_{\odot U}$ increases with $|t|$ and that there is a sensitivity of this observable to all four GPDs, especially at large $\mid t \mid$. We also display in this figure our calculation with the factorized ansatz for the t-dependence of the H GPD in order to illustrate the model-dependence of our results. Since this beam spin asymmetry is sensitive to the imaginary part of TCS+BH amplitudes, its GPD dependence is contained in the imaginary part of CFFs.

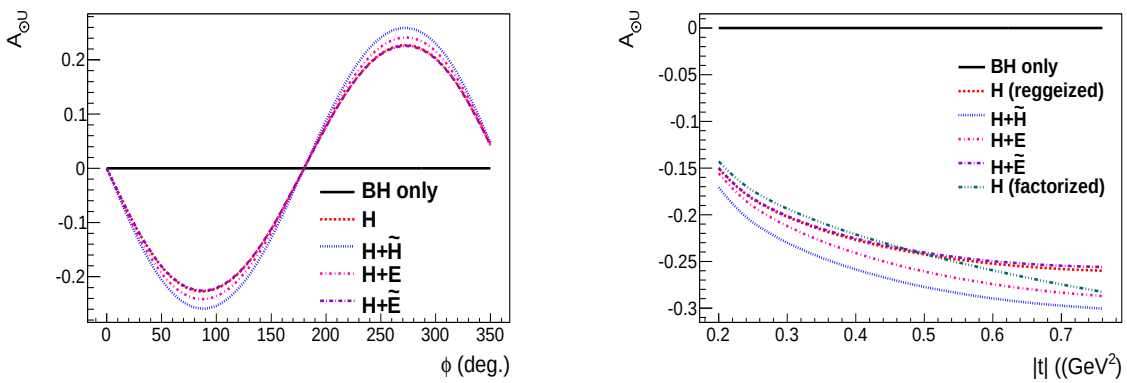

Figure 6: Left panel: The $A_{\odot U}$ for $\theta \in [45°, 135°]$ using differents GPDs parametrizations for TCS. The calculations are done for $Q'^2 = 7$ GeV^2, $\xi = 0.2$, $-t = 0.4$ GeV^2. Right panel: The $A_{\odot U}$ asymmetry as a function of t for BH+TCS at $\xi = 0.2$, $Q'^2 = 7$ GeV^2, $\phi = 90°$ and θ integrated over $[45°, 135°]$. TCS is calculated with different GPDs. From [].

2.2.3 Transversely polarized target spin asymmetries

We define the transversely polarized target spin asymmetries as

$$A_{Ui} = \frac{\sigma^+ - \sigma^-}{\sigma^+ + \sigma^-}, \tag{9}$$

where $\sigma^\pm$ stands for the 4-fold differential cross sections $\frac{d\sigma}{dQ'^2\, dt\, d\phi\, d(cos\theta)}$ for the two target spin orientations $+$ and $-$ along the axis $i = x, y$ or any other ϕ_S direction with $\theta_S = 90°$.

We show in Fig. 7 our results for the ϕ-dependence of A_{Ux} and A_{Uy} for $Q'^2 = 7$ GeV^2, $\xi = 0.2$, $-t = 0.4$ GeV^2 and for θ integrated over $[\frac{\pi}{4}, \frac{3\pi}{4}]$. The TCS is calculated with differents GPDs

parametrizations. We observe $\sin\phi$ or $\cos\phi$ shapes with amplitudes between 10 and 15%. Like for $A_{\odot U}$, the BH doesn't produce any asymmetry and any non-zero asymmetry directly reflects the strength of GPDs. We show in Fig. 8 the t-dependence of A_{Ux} and A_{Uy} at ϕ=90° and 0° respectively, for the kinematics $\xi = 0.2$, $Q'^2 = 7$ GeV^2 and θ integrated over $[\frac{\pi}{4}, \frac{3\pi}{4}]$. In this figure, TCS is calculated with different GPDs. Depending on the value of t, the two asymmetries are sensitive to the GPDs H, $\tilde{H}$ and E in various proportions. We also display in this figure our calculations with the factorized ansatz for the t-dependence of the H GPD in order to illustrate the model-dependence of our results. Experimentaly, we access different values of ϕ_S, which are taken into account in the calculation of the polarized cross sections for our projections. This dependence will be discussed in the next paragraph.

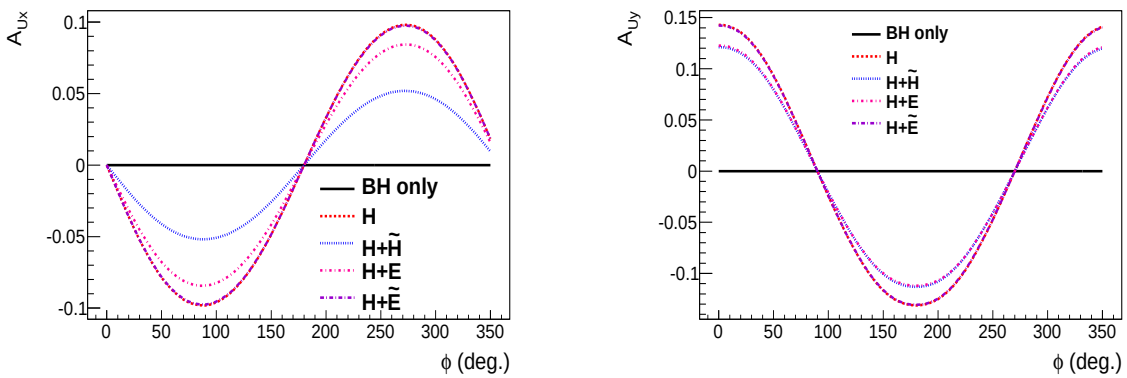

Figure 7: The A_{Ux} (left panel) and A_{Uy} (right panel) asymmetries as a function of ϕ for $\xi = 0.2$, $Q'^2 = 7\,\text{GeV}^2$, $-t = 0.4\,\text{GeV}^2$ and for θ integrated over $[\frac{\pi}{4}, \frac{3\pi}{4}]$. The TCS is calculated with differents GPDs parametrizations.

2.2.4 Relations between cross sections and Compton Form Factors for TCS and DVCS

Analytic equations have been developped for the unpolarized and circularly beam polarized TCS [**?**]. The squared TCS amplitude summed over the photons spin states is expressed as a function of CFFs [**?**] and is proportionnal to (using our notations)

$$TCS^2 \propto (1-\xi^2)\left(|\mathcal{H}|^2 + |\tilde{\mathcal{H}}|^2\right) - 2\xi^2 \Re\left(\mathcal{H}\mathcal{E} + \tilde{\mathcal{H}}\tilde{\mathcal{E}}\right), \tag{10}$$
$$-(\xi^2 + \frac{t}{4m_N^2})|\mathcal{E}|^2 - \xi^2 \frac{t}{4m_N^2}|\tilde{\mathcal{E}}|^2.$$

The dominant sin(ϕ) amplitude term (M^{--}) of the circularly beam polarized cross section decomposes into CFFs and FFs and is proportionnal to [**?**]

$$M^{--} \propto F_1\mathcal{H} - \xi(F_1+F_2)\tilde{\mathcal{H}} - \frac{t}{4m_N^2}F_2\mathcal{E}. \tag{11}$$

One can notice the similitudes with the DVCS polarized cross sections decomposition into CFFs (see the review [15]). However, the CFFs dependent terms in TCS observables are occuring with

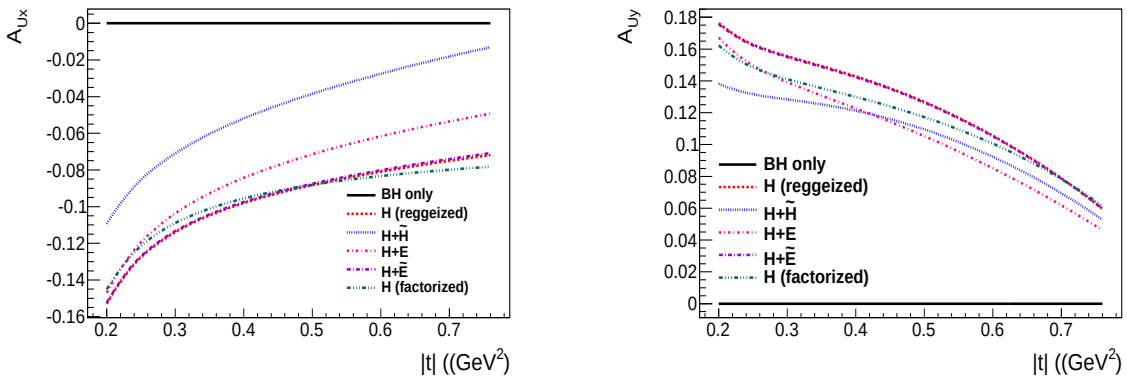

Figure 8: The A_{Ux} (left panel) and A_{Uy} (right panel) asymmetries as a function of t, at ϕ=90°, 0° and 90° respectively, and for $\xi = 0.2$, $Q'^2 = 7$ GeV^2, $-t = 0.4$ GeV^2 and θ integrated over $[\frac{\pi}{4}, \frac{3\pi}{4}]$. TCS is calculated with different GPDs.

different kinematical factors compare to DVCS. As demonstrated in [], the leading order and leading twist DVCS and TCS amplitudes are similar up to a change of sign of the imaginary part and a reversal of the photon polarization, which proves that DVCS and TCS depend on the same CFFs and carry the same information on GPDs. We therefore expect the DVCS and TCS observables being correlated at this order: the TCS unpolarized cross section is partially correlated to the DVCS one, the TCS circularly polarized beam spin asymmetries are correlated to the DVCS lepton beam polarization asymmetries and access the imaginary part of amplitudes, the DVCS and TCS single target spin asymmetries are correlated and access the imaginary part of amplitudes, the DVCS and TCS (with circularly polarized photon) double spin asymmetries are correlated and access the real part of amplitudes.

There is no reference displaying the CFF dependences of the transversely polarized TCS observables. Our calculation show a first order sin($\phi - \phi_S$) dependence of the single spin asymmetries which can be related to the DVCS ϕ and ϕ_S dependence of transverse target spin asymmetries (up to a sign change). DVCS phenomenology [16], results from the HERMES collaboration on transversely polarized DVCS, our results on GPD dependence of A_{UT} (Fig. **??**) suggest an enhanced sensitivity to $\Im\mathcal{E}$ from the (cos(ϕ)sin($\phi - \phi_S$)) moment of the transverse target spin asymmetry.

2.2.5 Higher order effects and impact on the observables

We neglected in the above discussion the impact of higher twist and next to leading order effects on the observables, and on the possibility to access the same CFFs with DVCS and TCS. Higher twist effects have been found to be non negligible from recent JLab DVCS experiments [**?**]. In TCS, we show in [12] that the impact on the observables is expected to be small compare to their GPD dependencies. However, these results didn't included all corrections and no experimental measurement has been published yet for TCS. Next to leading order calculations of DVCS+BH and TCS+BH show a different NLO structure for the two reactions [], and small but non negligible

effects are expected on the observables. While higher twist and higher order effects may not be suppressed at JLab kinematic, we expect them to not affect much our conclusions in regard to expected uncertainties on measured observables, and we expect being able to combine DVCS and TCS fits in a multi-observables CFFs fitting approach. If these effects are found to be large, we may observe some difference between DVCS and TCS. Some of the higher twist terms are of opposite sign, which may in this case provide a good opportunity to study these effects.

2.3 Extraction of CFFs from TCS measurements and impact for GPDs

2.3.1 Framework

We base the discussion in the current section under the assumption of negligible higher order and higher twist effects. In this case, we access the same CFFs from DVCS and TCS, and can either access the CFFs independently from the two reactions and compare the results, either combine DVCS and TCS observables to a multi-observable fitting.

We show in Fig. 9 the kinematical domain which can be accessed for DVCS and TCS. We display in blue the (ξ, Q'^2) phase space accessible for TCS with an 11 GeV electron beam, assuming that the real photon is provided by bremsstrahlung of the electron and that its energy is in $E_\gamma \in [5, 11]$ GeV. We have applied two cuts: $Q'^2 \in [4, 9]$ GeV^2 and $-t \in [0, 1]$ GeV^2. The motivations are respectively to stay in the region free of vector mesons resonances and minimize higher twist corrections to the TCS formalism, which grow with $\frac{t}{Q'^2}$. We overlap in red in this same figure the (ξ, Q^2) phase space accessible with an 11 GeV beam for DVCS. We have applied the cuts: $-t \in [0, 1]$ GeV^2, for the same reason as for TCS, and $s > 4$ GeV^2 in order to stay above the baryon resonance region. One notes the large intersection between the DVCS and the TCS phase spaces.

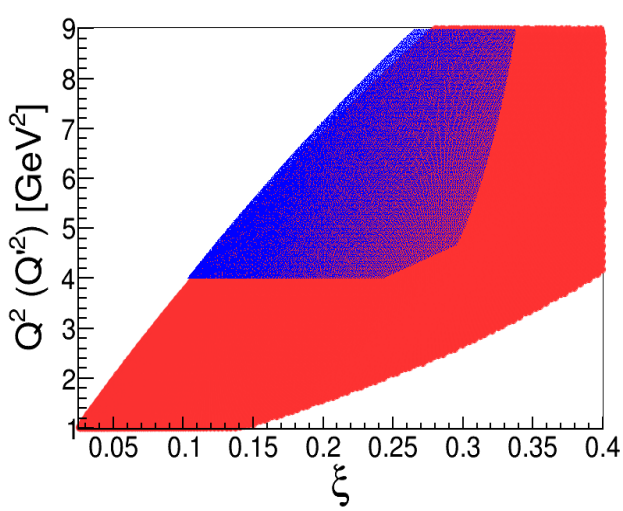

Figure 9: Kinematical domain accessible as a function of ξ and Q^2 for DVCS (red plain surface) and in ξ and Q'^2 for TCS (blue dotted surface) with an 11 GeV electron beam. For DVCS, the cuts $-t \in [0, 1]$ GeV^2 and $s > 4$ GeV^2 have been applied and for TCS, the cuts $E_\gamma \in [5, 11]$ GeV, $-t \in [0, 1]$ GeV^2 and $Q'^2 \in [4, 9]$ GeV^2 have been applied.

2.3.2 Fitting method

We generated DVCS+BH and TCS+BH pseudo-data sets based on VGG model GPDs and calculations [7, 8, 9, 4, 12]. The cross sections are calculated at the same t and ξ for DVCS and TCS: DVCS+BH distributions are generated at t=-0.2 GeV^2, $\xi = 0.15$, Q'^{2} = 2.5 GeV^2, E(beam) = 11 GeV, TCS+BH distributions are generated at t=-0.2 GeV^2, $\xi = 0.15$, Q^2 = 4.5 GeV^2, θ_{CM} = 90°. The distributions are presented as a function of 16 bins in ϕ. In case of transversally polarized proton, we generated the polarized cross sections at $\phi_S = 0°$ (spin along x-axis) and at $\phi_S = 90°$ (beam along y-axis). We extracted the CFFs according to the fitting method from [14]. In order to match the uncertainties expected in short term experiments at JLab, and to compare DVCS and TCS in the same conditions, we set relative errors of 5% per bin in ϕ for both DVCS+BH and TCS+BH unpolarized cross sections. We set relative errors of 7% per bin in ϕ for all the polarized cross sections. We assume the same uncertainties for both reaction in order to compare the sensitivities to CFFs, even though DVCS+BH can be measured with a better accuracy thanks to its larger cross section. The free parameters of the fits are the 7 Compton Form Factors: $\Im(\mathcal{H})$, $\Im(\tilde{\mathcal{H}})$, $\Im(\mathcal{E})$, $\Re(\mathcal{H})$, $\Re(\tilde{\mathcal{H}})$, $\Re(\mathcal{E})$, $\Re(\tilde{\mathcal{E}})$. Figures of the fitted distributions and more details are given in Appendix 7.

We performed fits on the sets of observables presented on table 1. For configurations 1 to 5, we systematically performed fits for DVCS and TCS independently, and combining both reactions. For the configurations 6, 6′, 6″, we fitted observables from DVCS, TCS, DVCS+TCS, respectively (the symbol "x" in the table indicate configurations that are not fitted). In the table we used the notations corresponding to DVCS observables: the first index "L" for designing DVCS+BH beam spin asymmetries should be replace by an index "$\odot$" in case of TCS (circularly polarized beam). We indicated experimental Halls in JLab who have experiments accessing the different observables. Some of these experiments are running or approved to run in a short term. However, the projected uncertainties of these experiments are not corresponding to the one assumed in this exercise, done in the purpose of comparing DVCS and TCS in the same conditions.

Set of observables	DVCS	TCS	DVCS+TCS	# independent obs. (DVCS/TCS/both)
1) σ, $\Delta\sigma_{LU}$	A, B, C	A, B, C	A, B, C	2/2/2
2) σ, $\Delta\sigma_{LU}$, $\Delta\sigma_{UL}$, $\Delta\sigma_{LL}$	B	-	-	4/4/4
3) σ, $\Delta\sigma_{LU}$, $\Delta\sigma_{UT}$ (x2)	-	C	-	4/4/4
4) σ, $\Delta\sigma_{LU}$, $\Delta\sigma_{UT}$ (x2) $\Delta\sigma_{UL}$, $\Delta\sigma_{LL}$	-	-	-	6/6/6
5) σ, $\Delta\sigma_{LU}$, $\Delta\sigma_{UT}$ (x2) $\Delta\sigma_{UL}$, $\Delta\sigma_{LL}$, $\Delta\sigma_{LT}$ (x2)	-	-	-	8/8/8
6) σ, $\Delta\sigma_{LU}$, $\Delta\sigma_{C}$	-	x	x	3 (DVCS)
6′) σ, $\Delta\sigma_{\odot U}$, $\Delta\sigma_{LU}$	x	D	x	3 (TCS)
6″) 2) of DVCS + 3) of TCS	x	x	B+C	6 (DVCS+TCS)

Table 1: First column: set of combined observables for DVCS, TCS and DVCS+TCS fitting. Second to fourth column: current and future experiments at JLab accessing these observables (letters indicate experimental Halls). Note that the projected uncertainties of these experiments are not corresponding to the one assumed in this exercise, done in the purpose of comparing DVCS and TCS in the same conditions. Fifth column: number of uncorrelated observables.

The extracted CFF uncertainties are presented on Fig. 10 (imaginary parts) and 11 (real parts).

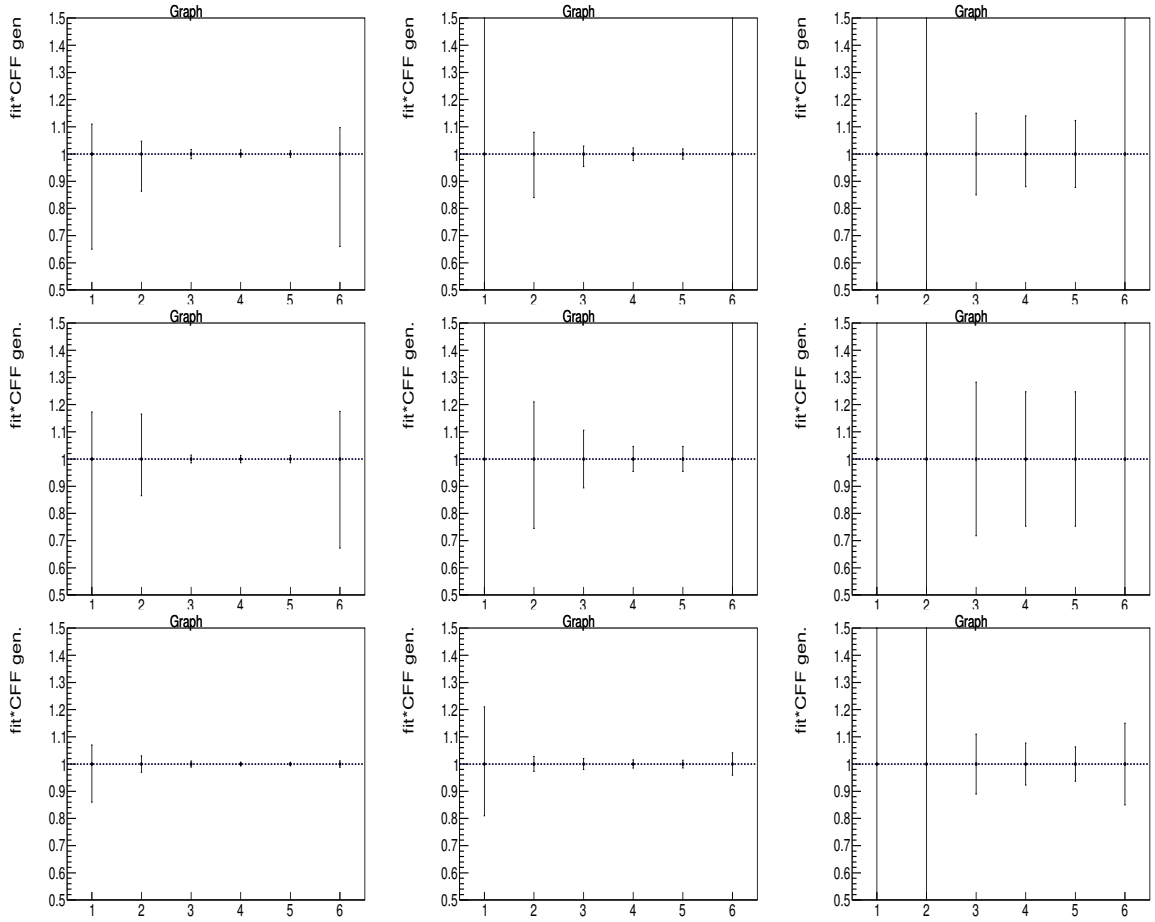

Figure 10: Extracted coefficients for imaginary part of CFFs, defined as fit result * generated CFF. Left column: Im($\mathcal{H}$), central column: Im($\tilde{\mathcal{H}}$), right column: Im($\mathcal{E}$). Top: extracted from DVCS, central row: extracted from TCS, bottom row: extracted from DVCS+TCS. Set of observable indices (from 1 to 6) are detailed in table 1. The scale is zoomed, fitting coefficient variation has been limited to $[-5, 5]$ time the generated one. Generated coefficient (1) is indicated by the black dashed line.

2.3.3 Interpretation on fitting DVCS or TCS independently

Measuring only the unpolarized cross section and beam spin asymmetry either from DVCS+BH or from TCS+BH (with a circularly polarized beam for TCS) allow for extracting $\Im\mathcal{H}$, $\Im\tilde{\mathcal{H}}$, and $\Re\mathcal{H}$ with a good enough precision for contributing to constraint GPD models and for comparisons between the two processes (Fig. 12). Having in addition the longitudinal target spin asymmetry allow for constraining better these CFFs, in particular $\Im\tilde{\mathcal{H}}$, and allow for bringing some constraint

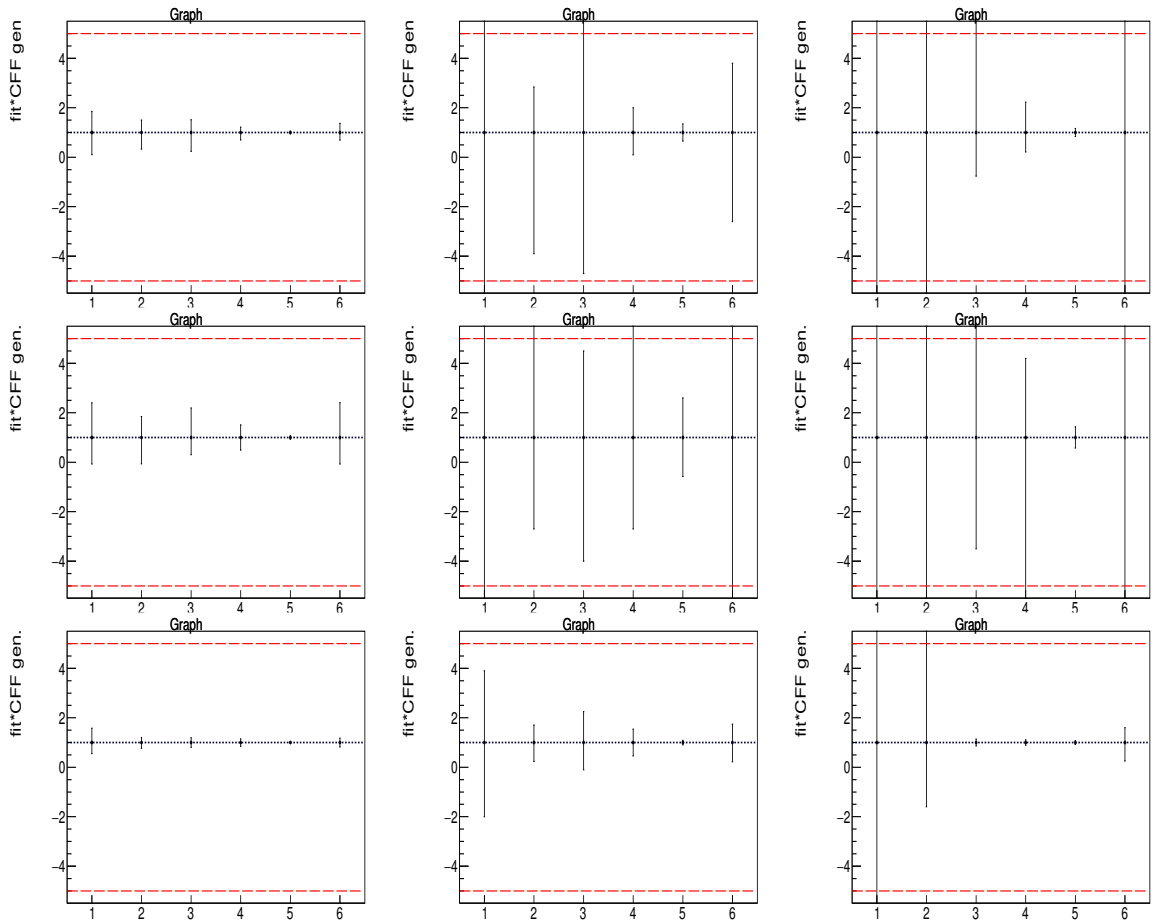

Figure 11: Extracted coefficients for real part of CFFs, defined as fit result * generated CFF. Left column: Re($\mathcal{H}$), central column: Re($\tilde{\mathcal{H}}$), right column: Re($\mathcal{E}$). Top: extracted from DVCS, central row: extracted from TCS, bottom row: extracted from DVCS+TCS. Set of observable indices (from 1 to 6) are detailed in table 1. Fitting coefficient variation has been limited to $[-5, 5]$ times the generated one. These limits are indicated by the red dashed lines. Generated coefficient (1) is indicated by the black dashed line.

on $\Re\tilde{\mathcal{H}}$.

Having in addition to the unpolarized cross section and to the beam spin asymmetry, the two independent transverse target spin asymmetry allow to constraint in addition $\Im\mathcal{E}$ (Fig. 12). Thanks to the correlations between the CFFs and the fact of having more independent observables to constraint the fits, a much better precision is reached for $\Re\mathcal{H}$ compared to cases without transverse target asymmetries (Fig. 12).

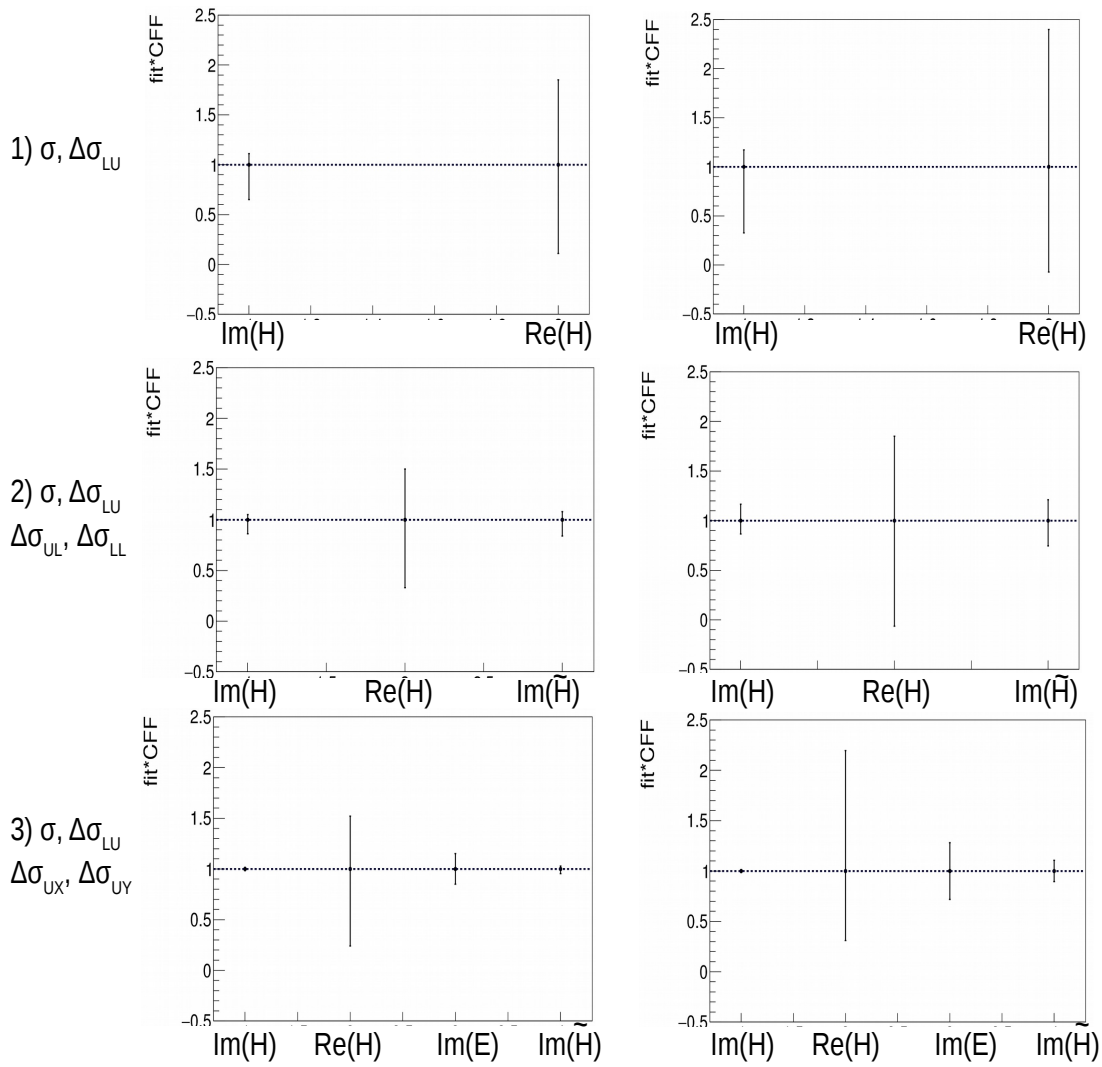

Figure 12: Extracted CFFs from DVCS (left column) and TCS (right column), using σ and $\Delta\sigma_{LU}$ (top row), using σ, $\Delta\sigma_{LU}$, $\Delta\sigma_{UL}$, $\Delta\sigma_{LL}$ (center row) and using σ, $\Delta\sigma_{LU}$, $\Delta\sigma_{UX}$, $\Delta\sigma_{UY}$ (bottom row).

Fitting DVCS+BH or TCS+BH unpolarized cross sections, beam polarized cross sections, 3 single target polarized cross sections (1 longitudinal, 2 transverse), and the double beam and longitudinaly polarized target cross sections (case 4) bring constraint to $\Im\mathcal{H}$, $\Im\tilde{\mathcal{H}}$, $\Im\mathcal{E}$, $\Re\mathcal{H}$, $\Re\tilde{\mathcal{H}}$ and $\Re\mathcal{E}$. Adding the double beam and transverse target spin asymmetries with the same precision (case 5)

will strongly shrink the uncertainties for all the CFFs and avoid incorrect solutions to the problem, thanks to it being overconstrained. The CFF $\Re\tilde{\mathcal{E}}$ is constrain thanks to correlations with other CFFs. This case is not corresponding to any short term DVCS or TCS experiments, and represent an ideal case of what can be achieved according to the uncertainties we set and the method.

We notice that in a scenario of same uncertainties on DVCS and TCS observables, the sensitivities to CFFs of DVCS observables are stronger the sensitivities of TCS observables. Indeed, TCS is more suppressed than DVCS compared to the associated BH process in the reaction. However, we can constraint CFFs from the two reactions independently and compare the results to demonstrate GPDs universality.

2.3.4 Interpretation on fitting simulteanously DVCS and TCS

In the first 5 data sets, we fitted simulteanously correlated observables from DVCS and from TCS. These simultenaous fits allow for about a factor of 2 reduction of error bars compared to the case of fitting only DVCS. This reduction is larger than statistically expected, due to the fact that the unpolarized cross sections are not fully correlated and therefore they bring both some new information. Combining observables from both reactions can help at a non negligible level in constraining GPD models by reducing uncertainty and allowing for extraction of CFFs which would be hard to constraint otherwise.

The 6″ data set is a combination of DVCS 2^d data set and TCS 3^d data set, corresponding to short term approved or proposed experiments at JLab. Independent information is brought by the different target polarization accessible in these experiments. Combining these data sets allow for constraining at the same time all CFFs.

Even thought simultenaous fits are assuming GPDs universality, they allow for bringing strong constrain to GPD models with short term upcoming DVCS and TCS experiments, compared to measurement from DVCS only.

2.3.5 Neutron measurements and flavor decomposition for the GPDs

The results of sec. 2.3.3 demonstrate the feasibility of accessing CFFs and GPDs for the proton from DVCS and TCS measurements. However, for interpretations, GPDs have to be decomposed into flavor, which is possible thanks to measurements of the GPDs of the neutron in other experiments [] in addition to the measurements off the proton. In particular, the CFF $\Im\mathcal{E}$ for the neutron is accessible with the unpolarized and the beam polarized DVCS cross section measurements [] and the longitudinaly polarized experiment [] using the CLAS12 spectrometer. As shown on Fig. 13, the neutron DVCS measurement will complement the TCS measurement we are proposing for the flavor decomposition of the GPD E, with uncertainties on the CFF at the same level.

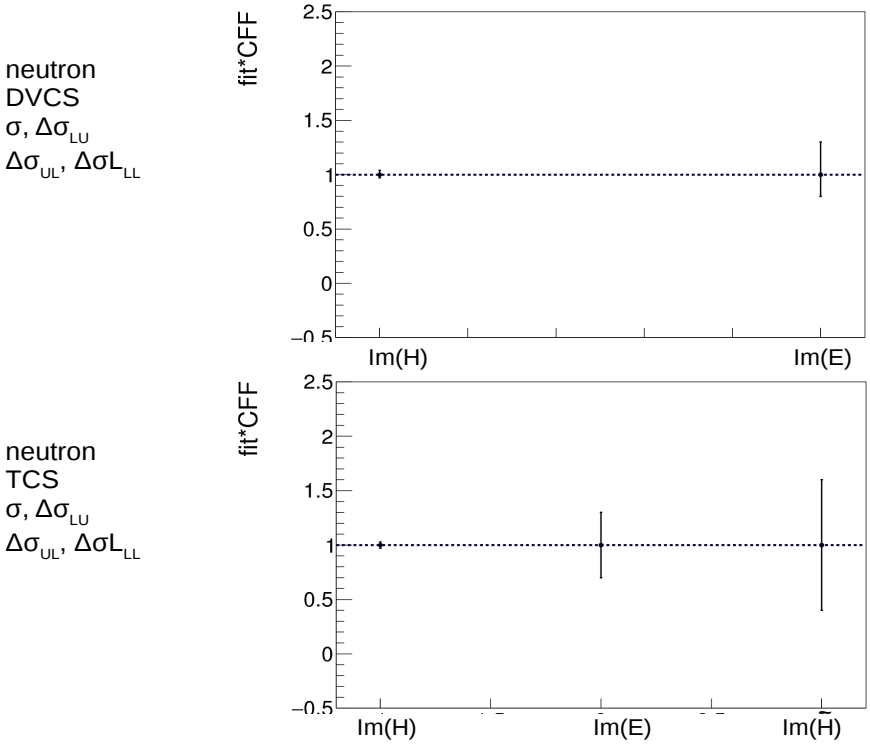

Figure 13: Extracted CFFs from DVCS (left column) and TCS (right column) off the neutron, using σ, $\Delta\sigma_{LU}$, $\Delta\sigma_{UL}$, $\Delta\sigma_{LL}$.

3 Experimental setup

3.1 The concept of setup

The setup is aimed at detection of decay lepton pair and recoil proton from BH/TCS events in triple coincidence, in forward kinematics. The key components of the setup are high intensity photon source, transversely polarized proton target, and a set of detectors for proton and lepton detection and identification.

The experiment will utilize untagged bremsstrahlung photon beam from Hermetic Compact Photon Source (CPS) ([32]) on the UVA polarized ammonia target ([28, 29]). The CPS is capable of delivering up to 1.5×10^{12} photons per second with primary CEBAF electron beam of 11 GeV energy and $2.5\ \mu A$ intensity, within the energy range from 5.5 to 11 GeV ([33]). The photon beam has clear advantage over the electron beam when using the polarized target: less heat load, higher polarization and less depolarization of the target material. This boosts figure of merit for the beam – polarized target combination by factor of ∼30. The luminosity for combination may reach $10^{35} cm^{-2} sec^{-1}$.

To provide transverse polarization, the UVA target assembly will be rotated by 90° around vertical axis. For this configuration the rendered angular acceptance is $\pm 17°$ horizontally, and $\pm 21.6°$ vertically. The exit beam pipe excludes from angular acceptance a conical region with opening angle of $6°$.

The proposed positioning of detectors opimizes coverage of the remaining angular acceptace in a feasably simple way (Fig.14). The detectors are positioned above and below the exit pipe and span from $6°$ to $21.6°$ vertically, and $\pm 17°$ horizontally. Small adjustments in this coverage due to deflections of the particles in the target magnetic field and background distributions are described below, in Sections 3.4 and 3.5. Positioning at 150 cm from target ensures reasonable transverse sizes of detectors.

The proposed detector package in its minimal configuration consists of hodoscopes for detection of proton, and electromagnetic calorimeters for detection of leptons. The hodoscopes have X and Y planes and measure both transverse coordinates.

The final state of the reaction contains two leptons and a proton, which will provide a coincidence trigger.

The exclusivity of the reaction is ensured by detecting all final-state particles, e^+e^-p and cutting on the missing-particle kinematics.

The proposed design characteristics of the detectors are presented in Table 2.

The following sub-sections contain more detailed description of the parts of setup, and studies on background conditions and trigger choices.

3.2 High Intensity photon beam

The proposed experiment will utilize untagged photon beam from Hermetic Compact Photon Source (CPS) proposed by G. Niculescu B. Wojtsekhowski [32]. The bremsstrahlung photons are

Parameters	Calorimeters	Hodoscope
range in ϕ	$\pm 17^o$	$\pm 17^o$
range in θ	6° - 21.6^o	6° - 21.6^o
	-6° - -21.6^o	-6° - -21.6^o
$\delta\phi$	< 5 mr	$< 1^\circ$
$\delta\theta$	< 5 mr	$< 1^\circ$
Energy resolution	$\sim 2\%/\sqrt{E}$	$\sim 10\%$
Time resolution	< 100 ps	< 100 ps
PID:		
e/π	~0.01	...
π/p	....	~0.1

Table 2: Proposed characteristics of the TCS detector setup. ϕ denotes angle in horizontal plane, and θ denotes angle in vertical plane.

produced from CEBAF electron beam (maximum energy 11 GeV) impinging on 10% Cu radiator. The electrons after target bend in 1 m long, 2.2 T field magnet, while photons pass straight through narrow, 2 mm in diameter collimator before reaching target. As bent electrons are dumped in specifically designed for that purpose body of magnet, the whole setup is heavily shielded by W-alloy in order to eliminate produced radiation.

The spot size of photon beam at 2 m away from the radiator is estimated to be ~0.9 mm. The projected photon flux is 1.5×10^{12} s^{-1} for primary electron beam current 2.5 μA, for photon energies $>$ 0.5 E_{beam} [33].

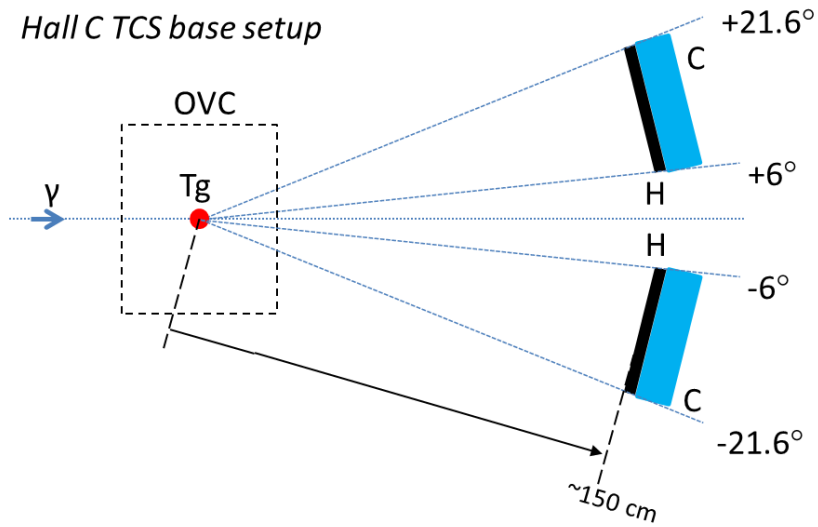

Figure 14: Side view of the TCS experimental setup. Shown are photon beam (γ), transversely polarized target (Tg) in the scattering chamber (OVC), and pairs of hodoscope (H) and calorimeter (C) counters for detection of the recoil proton and the lepton pair.

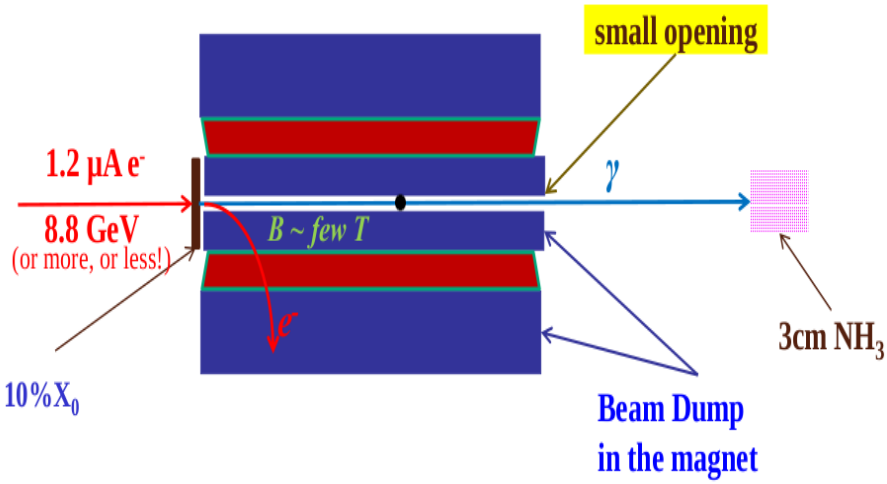

Figure 15: The conceptual design of Hermetic Compact Photon Source.

3.3 Polarized Target

Hall C has a long and successful experience with the use of solid polarized targets, starting in 1998 with the first run of E93-026[24] designed to measure the electric form factor of the neutron. This was followed by its second run in 2001 and immediately by the Resonance Spin Structure experiment, E01-006[25] in 2002 and by the Spin Asymmetries Experiment on the Nucleon (SANE)[26] in 2009.

These targets exploit a technique called Dynamic Nuclear Polarization (DNP) in which polarization is transferred from unpaired electrons in a dilute concentration of paramagnetic centers (introduced via irradiation at 80K or by chemical doping). At 5 T and 1K the thermal equilibrium of both species (proton and electron) is determined solely by Boltzmann statistics and can be written as $P = \tanh \frac{\mu B}{kT}$. The TE polarization of the electron under these conditions is 99.8% while the proton is 0.51%, the difference due solely to the size of their respective magnetic moments. The dipole-dipole interaction between the nucleus and the electron spins leads to hyperfine splitting. By applying a RF field with a frequency very close to the electron spin resonance frequency (about 140 GHz at 5.0 Tesla), the high electron polarization (due to the large electron magnetic moment) can be transferred to the proton.

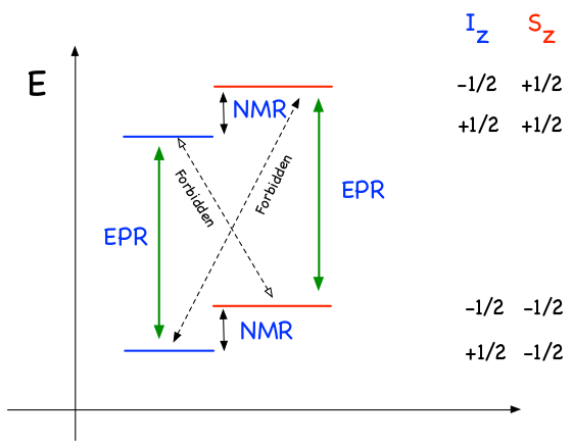

Figure 16: Transitions driven by GHz microwaves in the DNP process

In the case of the proton, the direct polarization enhancement is achieved by driving the transition from the ground state of $e_{\frac{1}{2}}p_{\frac{1}{2}}$ to the state $e_{\frac{1}{2}}p_{\frac{1}{2}}$ by applying microwaves with frequency around 139.914 GHz. See Figure 16.

The schematic view of the polarized target and the lower part of the target insert are shown in Fig. 17.

The target magnet is a pair of superconducting Helmholtz coils that when driven at 77 A produce a magnetic field of 5 Tesla. The coils have a 20 cm central bore, 100° opening angle and 8 cm of coil split. The field is uniform to 10^{-4} over 3 cm diameter right cylinder.

To provide transverse polarization of the target needed in this measurement, the target assembly will be rotated by 90° around vertical axis. Restricted by the magnet coils and scattering

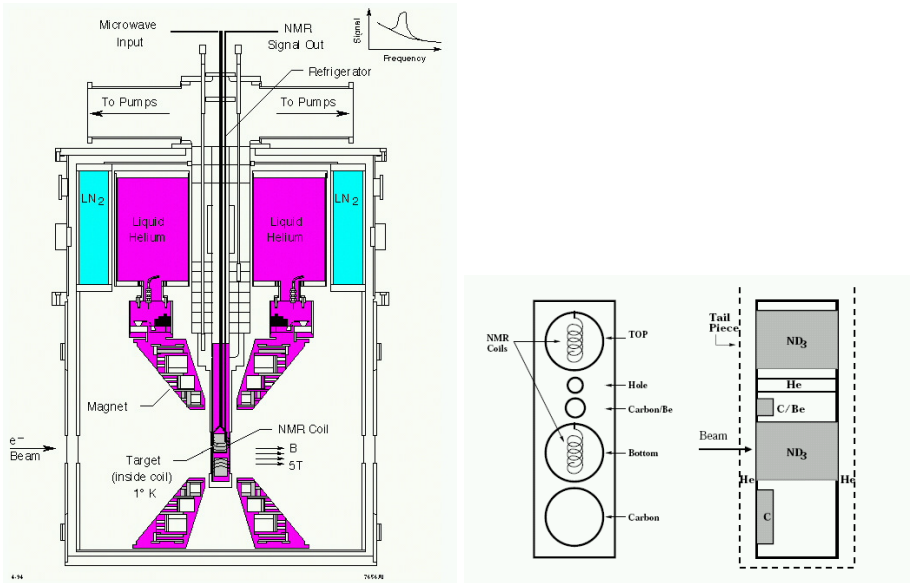

Figure 17: The UVA polarized target used in Hall C experiments. Left:Cross section view of the target. Right: A schematic drawing of the lower part of the target insert. The dashed line represents the tail piece which contained liquid helium during data taking.

chamber window, the angular acceptance in this configuration will span $\pm 17°$ horizontally and $\pm 21.7°$ vertically [1].

The target magnetic field direction has been found to be coincident with the geometric axis of the coils and is known to 0.1°[27]. The target is cooled by a ^4He evaporation refrigerator placed vertically in the center bore of the magnet. It is contained in a separate vacuum shield (see Fig. 17). The target material is held in cups at the the end of the target insert which can carry up to 5 targets: a top and bottom NH_3, an empty target and 2 solid targets (C or Be).

The microwaves are generated by an Extended Interaction Oscillator tube (Manufactured by CPI, Canada) which has a maximum power of ~20 W with approximately 1 W delivered to the target sample. $^{15}NH_3$ is chosen as the target material because of its high polarizability, large polarizable nucleon content and resistance to radiation damage.

The target polarization is measured via NMR using the Liverpool Q-meter in which the magnitude of polarization is linearly related with the voltage of the phase sensitive detector: $P = K \cdot S$, and K is a calibration constant. The calibration constant K is determined at thermal equilibrium. A series of NMR signal area measurements are made and averaged to obtain the calibration constant. They are typically done with each load of target material and as many time as is possible during the run, especially after anneals.

The target material consists of 1-3 mm diameter granules of NH_3, immersed a ^4He bath inside the target cavity. The packing fraction is the fraction of target cell volume filled by target material (NH_3), the rest of the cell being filled with liquid ^4He. The packing fraction is important for the

[1] A version of the target used in JLab Hall A g_p^2 experiment E08-027.

simulation of the scattering cross sections and for the determination of the dilution factor.

The dilution factor, f, is defined as the fraction of events originating from polarized hydrogen.

Interaction of beam with taget material causes a decay of polarization due to radiation damage caused by the build up of 'bad' paramagnetic centers. which allow more relaxation paths through the forbidden transitions. The decay of polarization continue until the measurement time for a given accuracy becomes unacceptable.

In practice, for experiments using 100 nA electron beam this can occur in about 8 hours. For experiments with photon beam like this one, the damage is less intence and the time is much longer. Fortunately, the process of annealing recombine the paramagnetic centers and restore polarization. To anneal the target material is moved out of the beam and the polarizing microwave radiation and is heated to between 70-100 K for between 10 and 60 minutes.

The detailed information about polarized target subsystems, technique of operation and experimental measurements can be found in Ref. [28, 29] and the UVa target group web server Ref.[30].

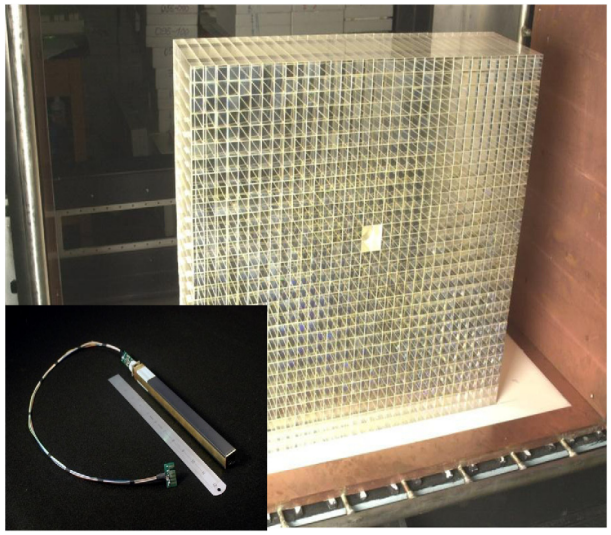

Figure 18: $2.05 \times 2.05 \times 18cm^3$ $PbWO_4$ crystals used in the high resolution part (HYCAL) of Hall B PrimEx experiment calorimeter [22].

3.4 Lepton detectors

The determination of the kinematic variables Q'^2, ξ and τ depends on the accuracy of reconstruction of the lepton energy and angle. Leptons (e^+ and e^-) in the experiment will be detected and identified by measuring their energies, and coordinates (X and Y) in a pair of electro-magnetic calorimeters.

The calorimeters are thought to be clone of the shower counter for the projected Neutral Particle Spectrometer. The basic concept for the NPS is a highly segmented electro-magnetic calorimeter preceded by a compact sweeping magnet. Experiments with NPS require detection of neutral particles with energies ranging between 0.5-7.6 GeV with good energy resolution ($\sim 2\%$), and good coordinate and angular resolution of 0.5-0.75 mrad, the latter is comparable to the resolutions of the focusing spectrometers in Hall C.

An assembly from lead tungstate crystals, similar to HYCAL calorimeter in the PRIMEX and PRIMEX-II experiments in Hall B [22] is recognized as a good match for the NPS calorimeter (see Fig 18). Preparation work for construction of the NPS calorimeter is well underway. Tests are being curried out at CUA and JLab to characterize optical and radiation-resistive properties of $PbWO_4$ crystals from SICCAS and other sources, a small prototype detector of 3×3 crystal assembly is construced for $insitu$ studies.

The new active divider design of the PMT bases provides a linear response up to high rates of $\sim$1 MHz. More information about the NPS and design studies can be found in reference [23].

The calibration procedures developed in Primex experiment can be adapted to this project. Experience with the HYCAL yielded energy and coordinate resolutions of $\sigma/E = 1.3\%$ and σ_x $\sim$1.28-2.10 mm at a neutral-pion energy of 5 GeV, giving an invariant mass distribution with a width of 2.3 MeV$/c^2$ (see Fig, 19). For comparison, an energy resolution of 2.2% for incident electrons of $\sim$4

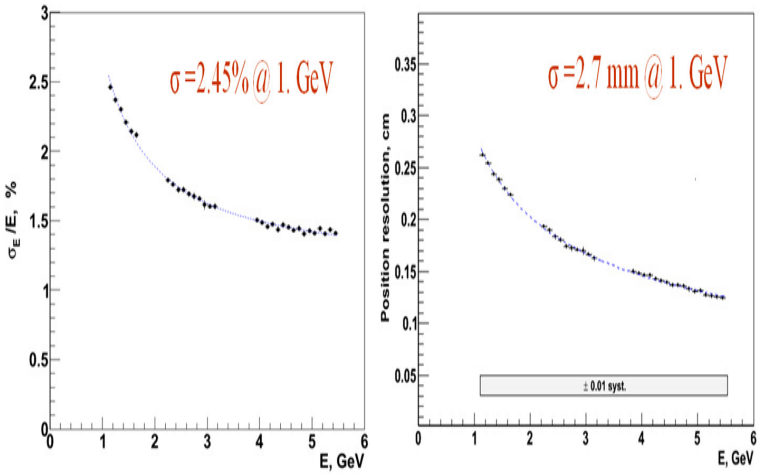

Figure 19: Energy and coordinate resolutions of $PbWO_4$ crystals based HYCAL calorimeter.

GeV energy has been obtained in beam tests with the prototype in Hall D at JLab.

The transverse size of the TCS lepton detectors is driven by required angular acceptance and distance to the target. Restricted by the target setup angular acceptance is $\pm 17°$ in horizontal plane and $\pm 21.7°$ in vertical plane (see Section 3.3). In addition, the beam pipe restricts scattering angles to greater than $6°$. Taken into account vertical deflections of the particles to be detected in the sideways magnetic field of the target, we consider positioning the lepton detectors above and below the beam pipe, at $0°$ of azimuthal angle.

Reasonable sizes for the detectors are obtained by positioning them at a distance ~1.5 m from the target. This implies $92 \times 41.5\ cm^2$ of active area, for the angular acceptances $\pm 17°$ horizontally and $\pm 15.7°$ vertically. For $PbWO$ crystals of $2.05 \times 2.05\ cm^2$ cross section for construction, the number of modules would be ~1000 for each detector (taken into account addition of a layer around the perimeter of cross-sectional area to exclude shower leaks). This number was refined after simulated acceptance studies, according to which a 50 $\times$ 23 matrix arrangement would be optimal, with 1150 blocks per detector. A further refinement took place due to background simulations, according to which the central region of detectors covering $\pm 1.6°$ horizontally must be excluded from consideration, because of unaceptably high background rates (see Section 3.6 below).

Hence the final layout of the calorimeters consists of 4 quarters (top left, top right, bottom left, bottom right), 23 $\times$ 23 matrix of blocks each, mirroring each other horizontally and vertically. The horizontal gap between left and right quarters is 8.2 cm wide, the vertical gap is 15.8 cm wide. The number of required lead tungstate crystals totals to 2,116.

3.5 Detection of recoil protons

Determination of momentum transfer -t and its resolution depends on accuracy of reconstruction of the recoil proton four momentum. Design requirements for the proton detectors are defined by kinematics, required accuracy, available space and cost, as well as by the expected background conditions. The recoil detectors will be located just before the lepton detectors and will cover a

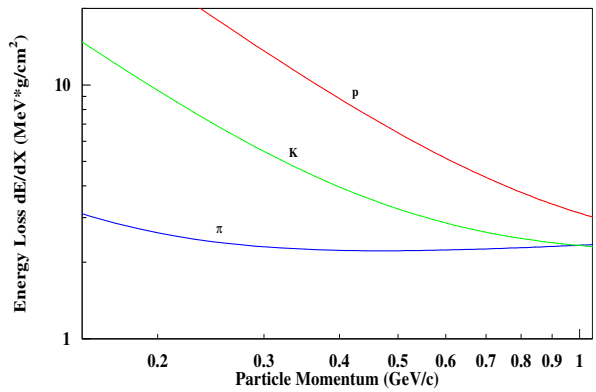

Figure 20: Proton PID by dE/dx in the Recoil Proton Detector. The graph shows ionization energy losses versus momentum for pions, kaons and protons.

slightly larger angular area than allowed by the polarized target. Similar to the calorimeters' case (see Section 3.4), the horizontal band from -6° to 6° and vertical band ±1.6° at the middle of the acceptance will be excluded, and the detector will be divided in 4 separate partitions.

The proposed 4 proton detectors have hodoscopic construction. Each hodoscope consists of X and Y planes, and cover rectangular area of $50 \times 48\ cm^2$. The counters will be made of scintillator bars. The width and thickness of the bars will be optimized for accuracy of the track coordinates' determination, and for particle identification capabilities of the detectors.

The detected proton momenta will be within $0.3 - 1.2\ GeV/c$ range, with bulk of statistics between 0.4 and 0.8 GeV/c. Proton identification will be based on dE/dx signal from the hodoscopes. Thickness of at least few cm will be needed for reliable separation of protons and lighter particles at momenta $\sim$1 GeV/c (Fig. 20).

3.6 Background and trigger studies

For experiments with open geometry setups backgrond conditions are of special importance. This experiment will utilize bremsstrahlung photon beam of intensity, potentially as high as 2×10^{13} photons per second on target of 3.8% radiation length. Simple PDG based estimates for e^+e^- γ-conversion production alone yields 3%/γ probability, i.e. rates in $\sim 10^{11} Hz$ range, even a small portion of which in the acceptance may cause difficulties.

A Geant4 based simulation code was developed to study background conditions, and detector acceptances as well. The code models target assembly (scattering chamber with its windows and shieldings, target cell and target material, magnet coils, magnetic field) and detector package. The background events in the detectors were generated by passing bremstrahlung photons through the target assembly. The photon energy was sampled from bremsstrahlung spectrum with tip energy

of 11 GeV.

A custom made, fast c++/Root code for acceptance studies was also helpful in this case. The code feutures point target, target magnetic field, target chamber and detector acceptances.

It was found that among background tracks within the detector acceptances 48% are γ-s, 24% are positrons and 28% are electrons. The hadron content is small. Energy deposition from background events in the calorimeters reaches 4 GeV (Fig.21). There is low energy background, with energies less than 100 MeV or so, which can be eliminated by posing cut of a few hundered MeV on the hit energies.

The transverse magnetic field from target deflects charged background toward detectors. The middle of acceptance, where backgeound rates are nontractable, is particularly affected (Fig. 22). Excluding horizontal angle range $\pm 1.6^\circ$ in the acceptace and making corresponding modifications in the detector setup (see Sections 3.4 and 3.5 sizeably reduces that region.

For construction of a viable low level trigger, identification of the ranges of useful events is necessary. For loose cuts on the TCS kinematic variables of interest $9\ GeV^2 > Q^2 > 4\ GeV^2$, $-t < 1\ GeV^2$, $s > 4\ GeV^2$, $-t/Q^2 < 0.3$, momenta of leptons from detected BH events are greater than 1 GeV, and sum of them is greater than 5 GeV. By establishing those thresholds on the deposited energies in the calorimeter, one can reduce rates of e^+e^- background coincident events by 3 orders of magnitude, but still leave them in $10^5\ Hz$ range (Fig. 24).

A more sofisticated trigger can be constructed based on that the sum of transverse momenta of the 3 detected particles are equal to 0. One can look for combinations of the measured quantities that are proportional to the transverse momenta, are easy to implement in the trigger, and construct the sum. For instance, the X component of the lepton transverse momentum can be represented by X coordinate of the hit cluster in the calorimeter, weighted by the energy of the cluster E. Then, assuming one lepton hit the top calorimeters, another the bottom calorimeters, one can look for a pair of hit clusters with significant energy depositions, calculate the energy weighted coordinates for them, and take the sum of the two quantities as a represenation of the transverse momentum

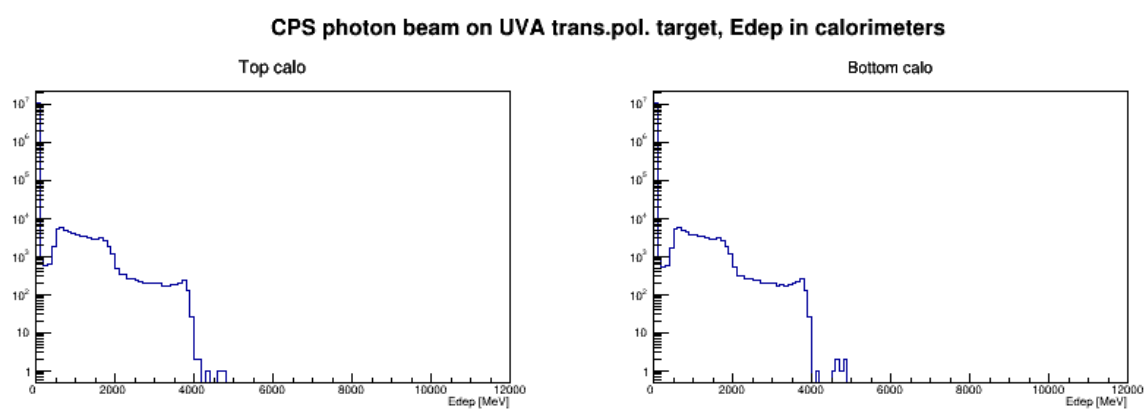

Figure 21: Background energy deposition in the calorimeters.

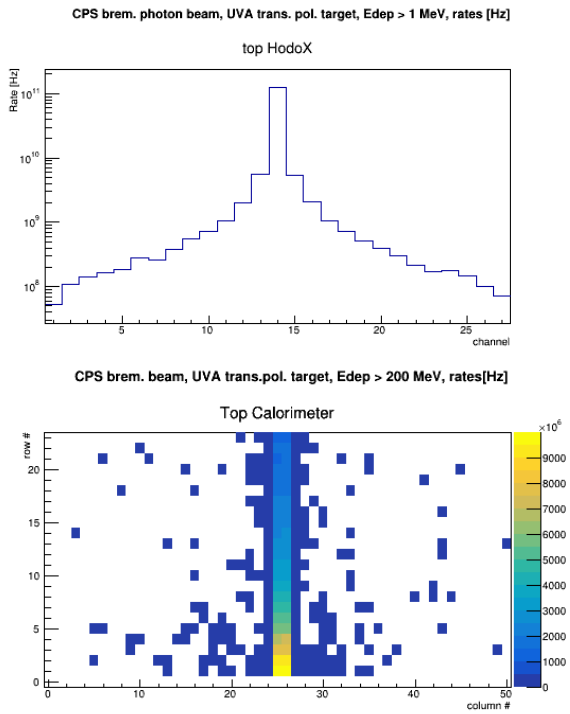

Figure 22: Left: background rates in the paddles of X hodoscope. The scintillator paddles are 1 cm thick, 4 cm wide. Hits with deposited energies greater than 1 MeV are counted. Right: background rates in the modules of top calorimeter. Hits with deposited energies greater than 200 MeV are counted.

of the decayed outgoing photon:

$$P_X(\gamma^\star) \sim X_+E_+ + X_-E_- \tag{12}$$

The same procedure can be applyed to the Y coordinate, but with taking into accout a caveat: contrary to the previous case, the leptons bend in axis direction. This results in a constant term in the expression for the sum:

$$P_Y(\gamma^\star) \sim Y_+E_+ + Y_-E_- + const \tag{13}$$

Such constructed quantities for the triple coincidence BH/TCS events are constained within ranges of ± 50 $GeV{\cdot}cm$ (X componemt), and from -100 $GeV{\cdot}cm$ to 50 $GeV{\cdot}cm$ (Y componemt) (Fig.25). The dips in distributions correspond to gaps between parts of the calorimeters' assembly.

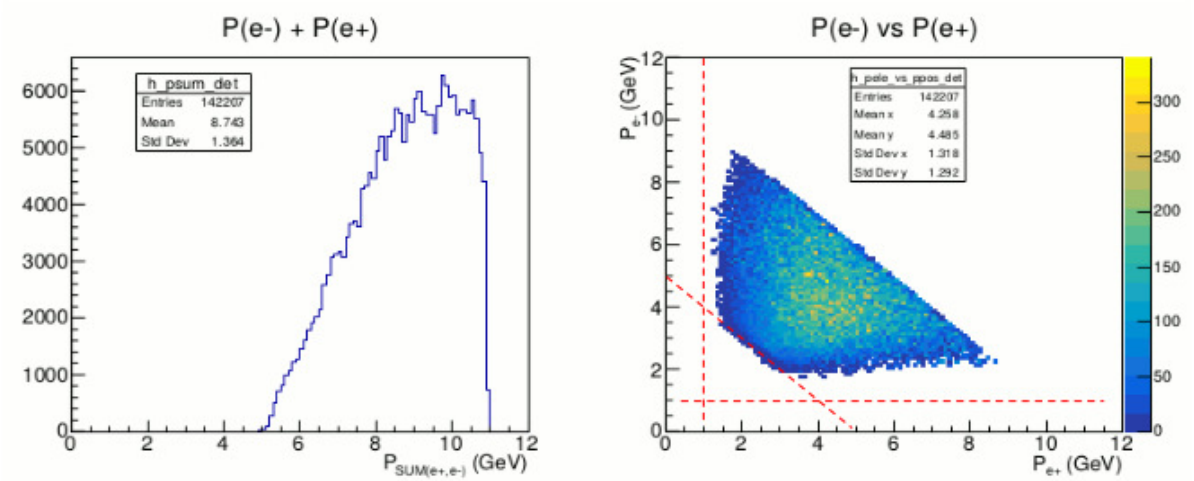

Figure 23: Lepton momenta of Bethe-Heitler events within acceptance of the TCS setup. Left: Sum of the momenta. Right: electron momentum versus positron momentum. The dashed lines indicate threshols on the electron and positron momenta greater than 1 GeV, and sum of the two greater than 5 GeV.

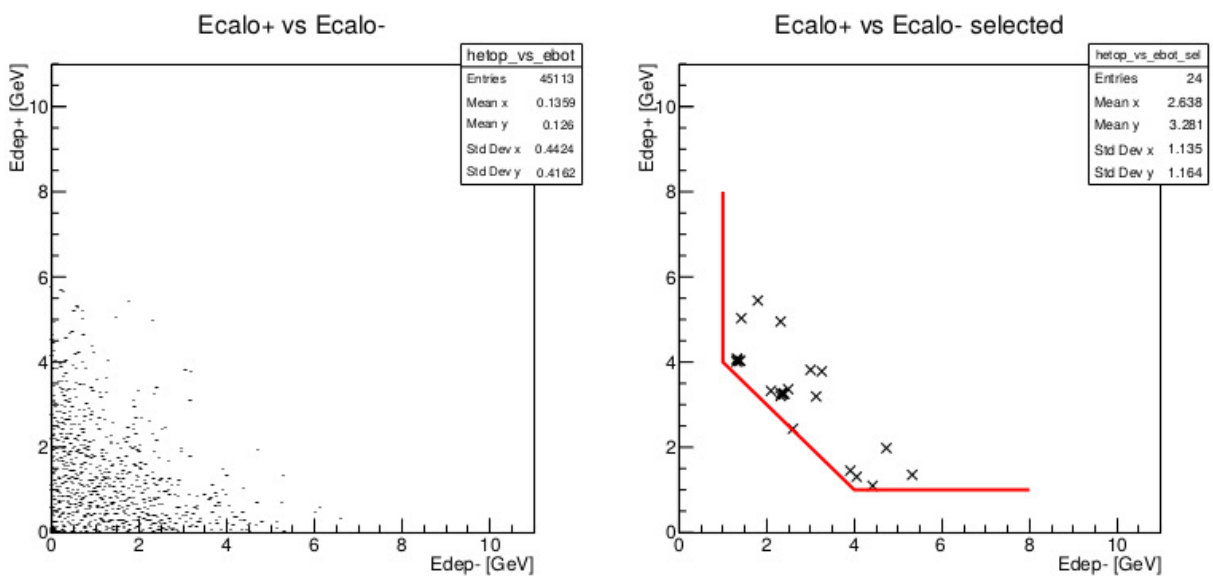

Figure 24: Bacground coincidence events in the calorimeters. Left: energy deposition in the top calorimeter versus energy deposition in the bottom calorimeter. Right: same for events surviving threshod cuts on the deposited energies.

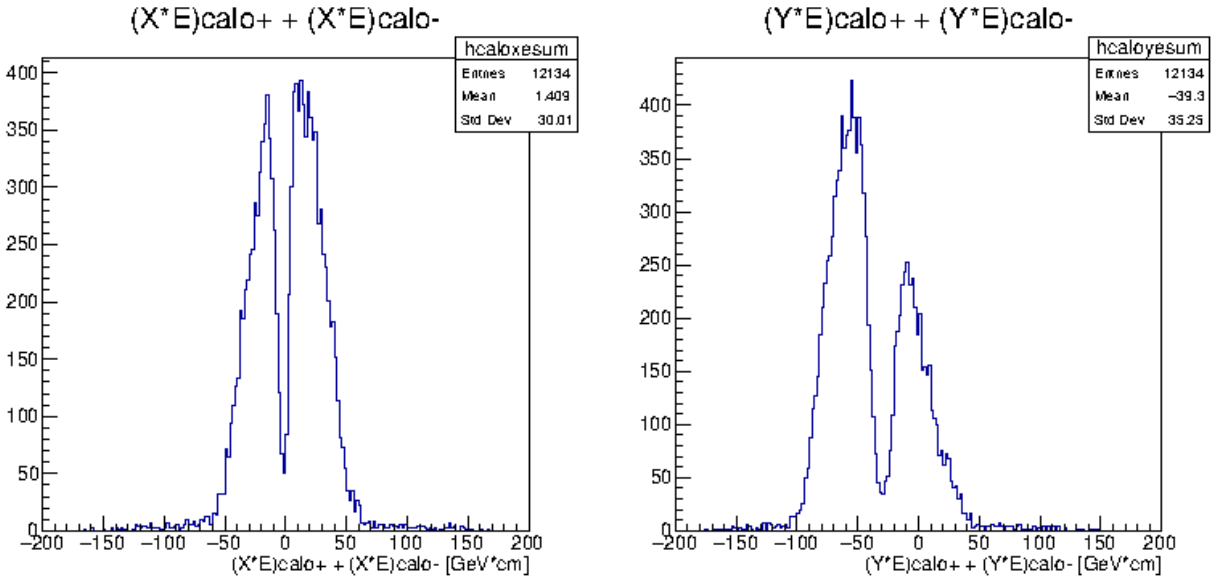

Figure 25: Weighted by deposited energy coordinates of hit clusters from leptons hitting the calorimeters, for BH/TCS events detected in the setup. Left: sum of the weighted X coordinates from top and bottom calorimeters. Right: same for the Y axis. See text for details.

4 Simulation studies from generated events

4.1 Event generator for the beam and target polarized TCS+BH reaction

We developed an event generator based on the formalism presented in 2.1. The generator webpage is hosted in [34], with a public version available. We generated events initiated from a real photon, which energy distribution is rescalled following a bremstrahlung spectra. At the generation level, we assume 100% polarization of the initial electron and 100% polarization of the target, which can be rescaled by dilution factors at the analysis level. We set the polarization of the target being along the x-axis, and we rotate randomly the reaction plane for taking into account the ϕ_S dependence of the reaction. The events are generated in the following kinematic range:

- 7.5 < E_γ<10.5 GeV,
- 4 < Q'^2 < 9 GeV^2,
- .04 < -t < 0.8 GeV^2,
- 40° < θ < 140°,
- 0° < ϕ < 360°,
- 0° < ϕ_S < 360°.

Fig. 26 shows the correlations between t, Q'^2 and ξ for all generated events.

These simulations are used for all projection studies in the following. Events are weighted according to the unpolarized and polarized TCS+BH, BH "only" and TCS "only" cross sections for the purpose of systematic studies. Unpolarized, beam or target polarized TCS+BH cross sections are used for the projection of experimental uncertainties.

Some studies in the above section are done with the genTCS [31] event generator, which use bremsstrahlung photons from 11 GeV primary electron beam within energy range 5.5 – 11 GeV, and point-like target, with invariant masses of the lepton pairs in the resonance-free region between 2 and 3 GeV.

4.2 Peaks in BH angular distributions and interpretations of the ϕ and θ dependence of the cross sections

Angular dependence of the lepton pair production can be understood with the BH propagators of eq.6. In the lab frame or in the γN CM frame, if one of the leptons are emitted along the beam direction, one of the terms becomes very large. It is then proportional to $\approx \frac{1}{m_e}$ (m_e is the lepton mass). At these limits, one of the two BH diagrams is largely dominant compared to the other one. One of the leptons takes most of the energy of the virtual photon and is emitted at very low angle ($\sim 0°$), while the other one is emitted at large angle ($\sim 180°$) with a very low momentum. The cross section drastically increases next to these limits and sharp peaks are observed in angular distributions. Azimuthal distributions (ϕ_{CM}) are also strongly affected by this effect: one lepton going to the beam direction is forcing all particles to be emitted in the same plane (see Fig. 4).

We expressed the cross sections as a function of the virtual photon CM frame electron angles ϕ_{CM} and θ_{CM} (eq. 2). The angle ϕ_{CM} is conserved in the boost from γN CM frame, θ_{CM} (boost axis, electron polar angle) is correlated to θ_{lab} for a given $\Theta_{\gamma\gamma^*}$ angle (angle between incoming and outgoing photon). At small $\Theta_{\gamma\gamma^*}$ (t_{min} limit), we have the following effect:

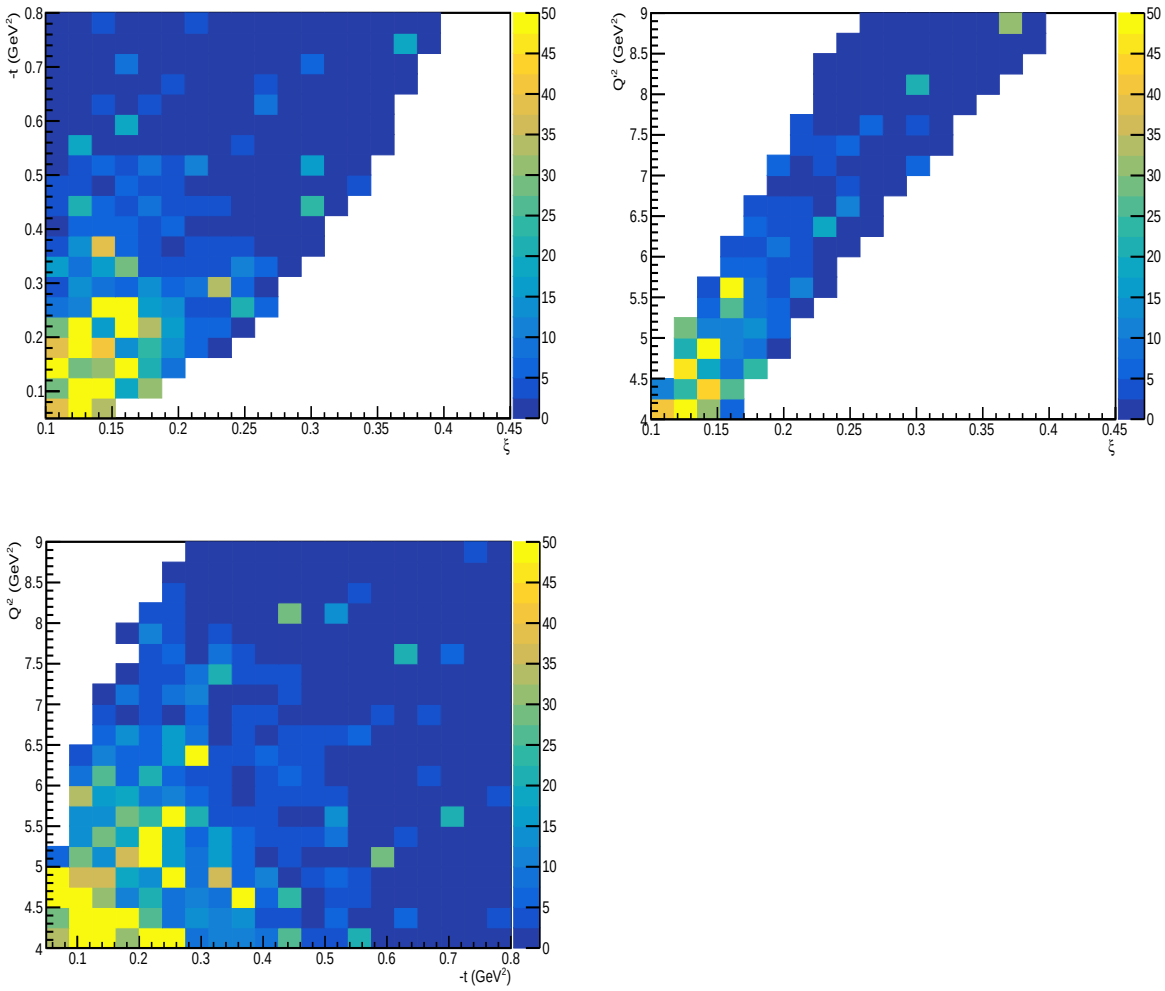

Figure 26: Top left: -t as a function of ξ, top right: Q'^2 as a function of ξ, bottom left: Q'^2 as a function of -t. The beam energy has been limited to $8.5 < E_\gamma < 10.5$ GeV. The weights are proportionnal to the unpolarized cross section.

- $\theta_{CM} \to 0$, i.e. e^- is emitted along the beam direction, the diagram on right panel on Fig. **??** largely dominates. A sharp peak will be observed in the cross section at $\theta_{CM} \to 0°$ and $\phi_{CM} = 180°$.
- $\theta_{CM} \to 180°$, i.e. e^+ is emitted along the beam direction, the diagram on left panel on Fig. **??** largely dominates. A sharp peak will be observed in the cross section at $\theta_{CM} \to 180°$ and $\phi_{CM} = 0°$.

At $\Theta_{\gamma\gamma^*}$ larger than zero, the position of the peaks in θ_{CM} distribution depends on the kinematics (E_γ, t, Q'^2). The correlation between $\Theta_{\gamma\gamma^*}$ and t and Q'^2 at fixed E_γ is displayed on Fig. 27.

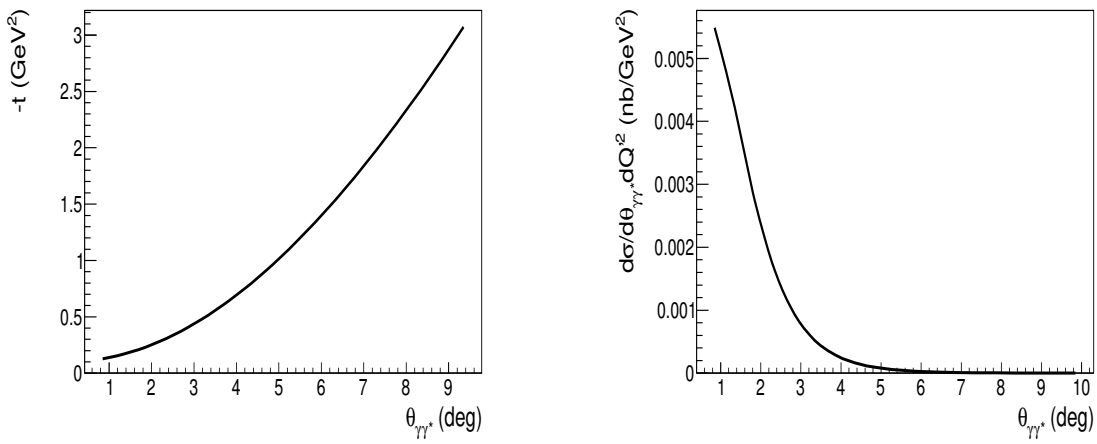

Figure 27: Distribution in -t versus $\theta_{\gamma\gamma^*}$ (left panel, at Q'^2=5 GeV^2) and BH cross section as a function of $\theta_{\gamma\gamma^*}$ (right panel, at -t=0.3 GeV^2 and Q'^2=5 GeV^2). Both curves are calculated at E_γ=9.5 GeV. for $0 < \phi_{CM} < 360°$ and $45° < \theta_{CM} < 135°$.

The effect of correlations between θ and ϕ at the JLab kinematics is illustrated on Fig. 28, presenting distributions in ϕ_{CM}, where θ_{CM} has been integrated in asymmetric ranges over θ_{CM} (one diagram dominates). At these kinematics, the BH peaks are at $\theta_{CM} \sim 20°$ and $\theta_{CM} \sim 160°$, explaining that the curve corresponding to $20° < \phi_{CM} < 30°$ presents the largest cross section. In the perspective of experimental measurements, integrating calculations over a symmetric range around $\theta_{CM} = 90°$, away from BH peaks, presents the advantage of having the same contribution from the two diagrams in the integrated cross section while enhancing the statistic in each bin for displaying distributions in other variables in the data.

Indeed, the θ_{CM} distribution and position of BH peaks is correlated to the angle $\Theta_{\gamma\gamma^*}$, which depends on t, Q'^2 and E_γ. For kinematics with $-t \to t_{min}$, the peaks are observed at $\theta_{CM} \to 0$ and $\theta_{CM} \to 180°$. For larger $-t$, and for different values of Q'^2 and E_γ, the peaks are observed at different values, approching $90°$ for the large -t limit. BH peaks are at $\theta_{CM} \to 0$ and $\theta_{CM} \to 180°$ when approching t_{min}, and at values between these two extrems limits for larger values of $-t$. We also observe that the sharp increase of the cross section next to the peaks is limited for larger value

of $-t$. At t_{min}, the cross section can increase by several orders of magnitude within a few degrees in θ_{CM} or ϕ_{CM} range.

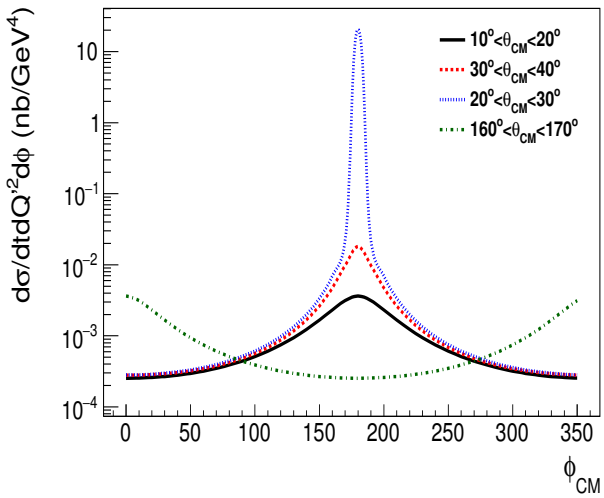

Figure 28: BH cross section as a function of ϕ at Q'^2 = 5 GeV^2, -t=0.3 GeV^2, E$_\gamma$=9.5 GeV, and integrated over θ_{CM} on various ranges (colored curves).

4.3 Impact on the analysis and solutions

While BH cross sections can be calculated for any kinematic or angular fixed values, a discretized problem with limited bin width will be affected by the very fast increase of the cross section next to the peaks in the angular distributions. While a sufficient amounts of simulations can be generated in order to achieve a reasonable precision for predicted cross sections from Monte-Carlo. However, experimental data are limited in statistics, and the exact kinematics of the events are known only up to the resolution precision. Experimental data are naturally "integrating" the cross section over a certain bin width, which cannot be thinner than the resolution in different variables. To fit these data, we need to integrate cross sections over the width of the bins they are presented into. As a consequence, it is not possible to achieve comparison with reasonable systematic uncertainties between experimental data having limited statistics and calculations when the cross sections are variating very fast over a single bin. Therefore, for fitting data with BH calculations, we have to stay away from BH peaks in the (θ_{CM}, ϕ_{CM}) distribution, where cross sections are typically increasing by more than two orders of magnitude within a single bin.

To reproduce experimental conditions (limited statistics, broad kinematic range) and get the position of the BH peaks, we computed BH cross sections as a function of θ_{CM} at fixed values of E$_\gamma$, t and Q'^{2}. We integrated the cross sections over ϕ_{CM} with a limited number of steps. We perfomed calculations for two values of θ_{CM} symmetric around $\theta_{CM} = 90°$ with 5° steps in θ_{CM}:

85° and 95°, 80° and 100°... The results are expected to be the same for the two symmetric values of θ_{CM}. We set as a condition to position the peaks and determine the region where we cannot fit data with reasonable errors, the observation of results being different by more than 5% (due to our binning and the fast variations). It defines the values of θ_{min} and θ_{max}, respectively the starts of the two steep slopes in θ_{CM} distribution. We reproduced the same exercise for different values of E_γ, t and Q'^2. Values of θ_{max} for $E_\gamma = 9.5$ GeV, as a function of $-t$ and Q'^2 are displayed on Fig. 29.

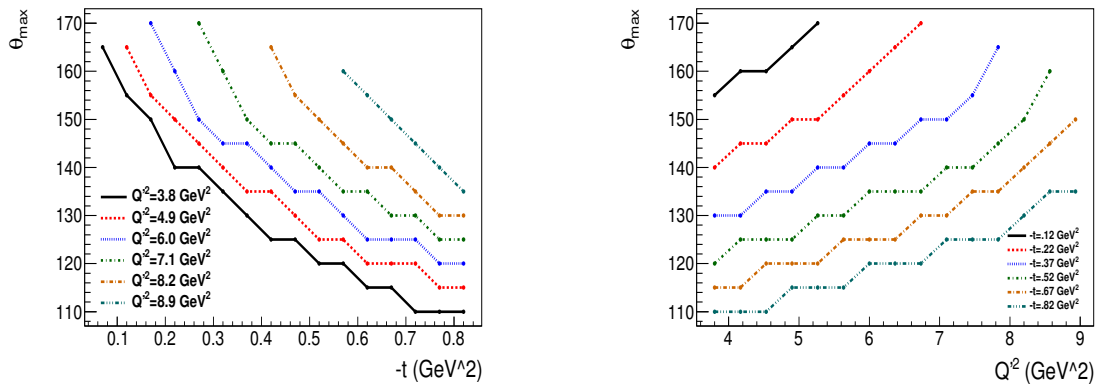

Figure 29: Values of θ_{max} for a fix beam energy $E_\gamma = 9.5$ GeV, as a function of t for different values of Q'^2 (top panel) and as a function of Q'^2 for different values of $-t$ (bottom panel).

We reproduced the same exercise by integrating cross sections over different ranges in ϕ_{CM} ($0\pm10°$, $0 \pm 20°$, $180° \pm 30°$...). We conclude that the peaks can be avoided by 2-dimensional cuts in ϕ_{CM} and θ_{CM}, which we appy in our projections, such as:

- if (θ_{CM}<θ_{min} and $150° < \phi_{CM} < 210°$), the event has to be rejected,
- if (θ_{CM}>θ_{max} and $-30° < \phi_{CM} < +30°$, the event has to be rejected,
- otherwise the event can be kept and results can be fitted with reasonnable systematic errors.

4.4 Correlation between the electron and the positron kinematics in the lab frame at vertex

We display in Fig. 30 the asymmetries between angles (θ_{lab}, ϕ_{lab}) and momentum (P_{lab}) of the electron and the positron in the lab frame. Equivalent 2D distributions are shown Fig. **??**. We defined these asymmetries, for θ_{lab} (and similarly for the other variables) as

$$\frac{\Delta\theta_{lab}}{<\theta_{lab}>} = \frac{\theta_{lab}(e^-) - \theta_{lab}(e^+)}{\theta_{lab}(e^-) + \theta_{lab}(e^+)}. \tag{14}$$

The $\frac{\Delta\theta_{lab}}{<\theta_{lab}>}$ and $\frac{\Delta P_{lab}}{<P_{lab}>}$ distributions are reflecting the interpretations of section 4.2: if one lepton takes more energy, it is scattered at lower angle with larger momentum while the other one is scattered at large angle with lower momentum. Therefore, these distributions will present maximal

asymmetries for larger cross sections. The $\frac{\Delta\phi_{lab}}{<\phi_{lab}>}$ distribution peaks at $\phi_{lab} = \pm 0.5$ are correlated to these asymmetric decays.

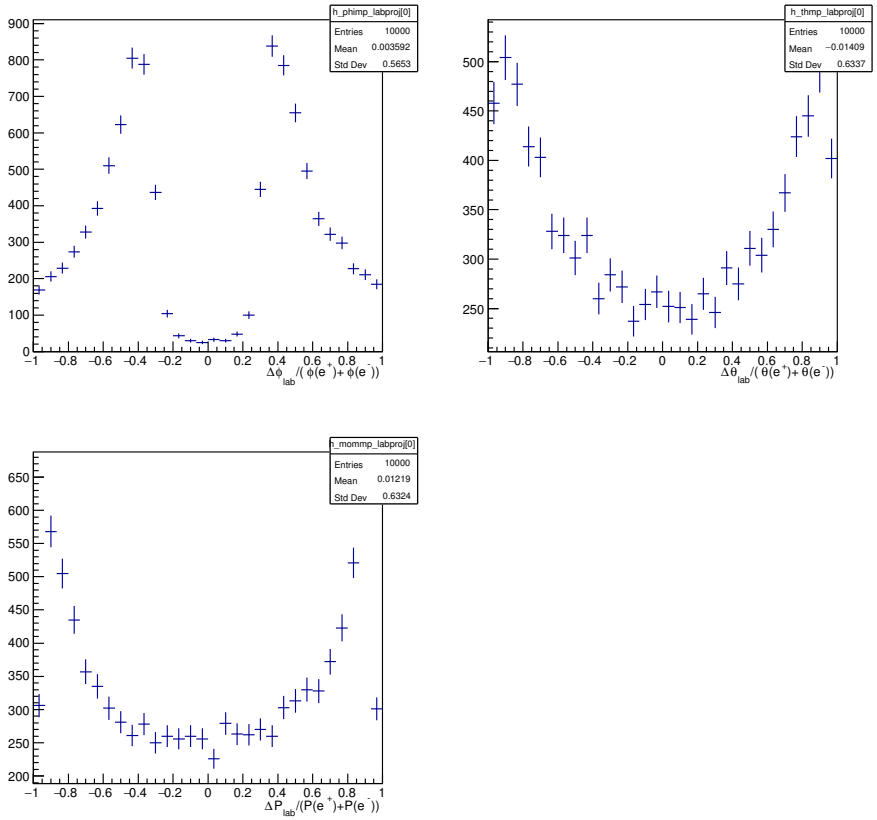

Figure 30: Asymmetries in lab frame between the scattered electron and positron. Top left: $\frac{\Delta\phi_{lab}}{<\phi_{lab}>}$, top right: $\frac{\Delta\theta_{lab}}{<\theta_{lab}>}$, bottom left: $\frac{\Delta P_{lab}}{<P_{lab}>}$.

We display on Fig. 33 θ ("physics" polar angle) versus θ_{lab} (in lab frame, at vertex) distribution of generated events for the scattered electron. The distributions are averaged over all kinematic variables but θ_{CM}. The weights are proportional to the cross section: the higher cross sections (color = yellow) observed in the lowest bin in θ_{lab} correspond to the BH peak for the electron scattered along the beam direction. The higher cross sections for larger θ_{lab} are a consequence of the correlation with the other BH peak: if the positron takes most of the available energy, the electron is scattered with lower momentum at larger lab angle ($\theta_{lab} \rightarrow 180°$).

4.5 Final particle distribution and physics impact as a function of the kinematics

As a consequence of the BH cross section behavior, it is not possible to conclude for the best position of the calorimeters and the recoil detector from the expected counting rates. Indeed, the cross section can be very large for some specific angles and momentum of the final particles, but the asymmetry and the TCS/BH rate may be small. We studied the angular and momentum dependence of the unpolarized cross section, the TCS/BH rate and the size of the asymmetries Figs. **??**

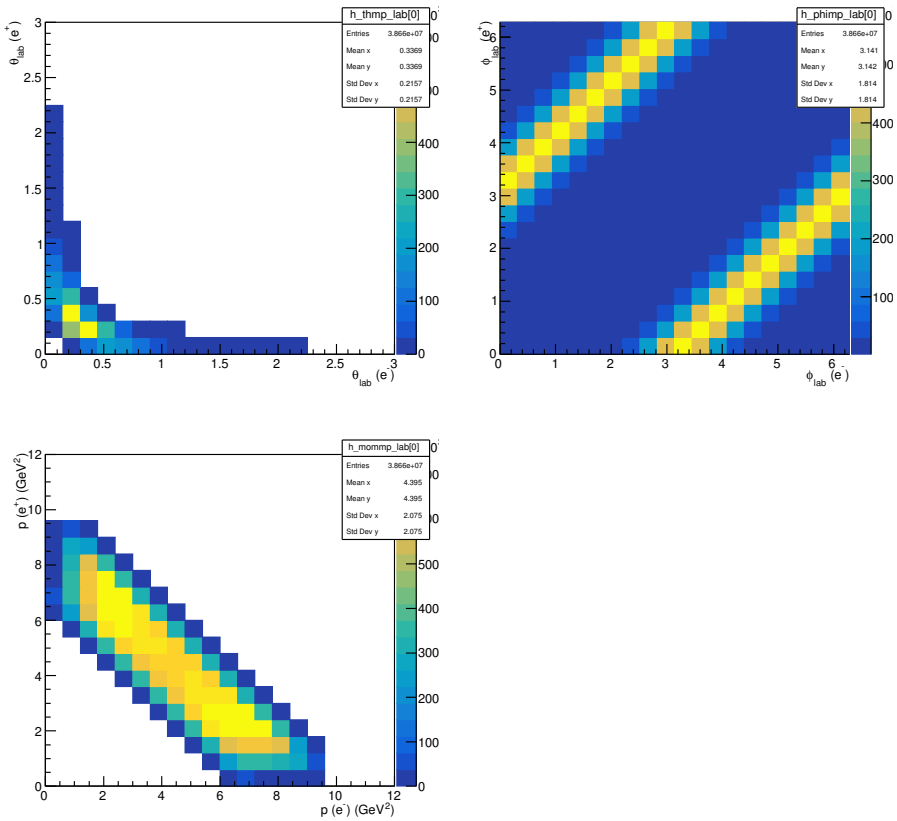

Figure 31: Top left: $\theta(e^+)$ versus $\theta(e^-)$ in lab frame, top right: ϕ(e$^+$) versus ϕ(e$^-$) in lab frame, bottom left: p(e$^+$) versus p(e$^-$) in lab frame.

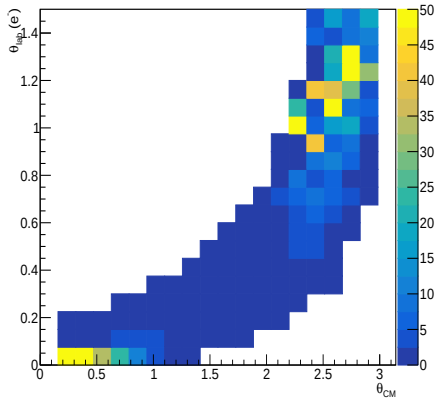

Figure 32: Distribution of θ_{CM} versus θ_{lab} for the scattered electron. Monte-Carlo data.

and **??** compares the 2D distributions of the electron and the proton momentum versus their polar angle (without deflection), weighed by factors proportionnal to the unpolarized cross section, the TCS/BH rate and the size of the transverse spin asymmetries. We concluded that the position of the detector in the proposed setup allows for a fair balance between counting rates, the size of the asymmetries and impact of the physics (shown by fitting the CFFs).

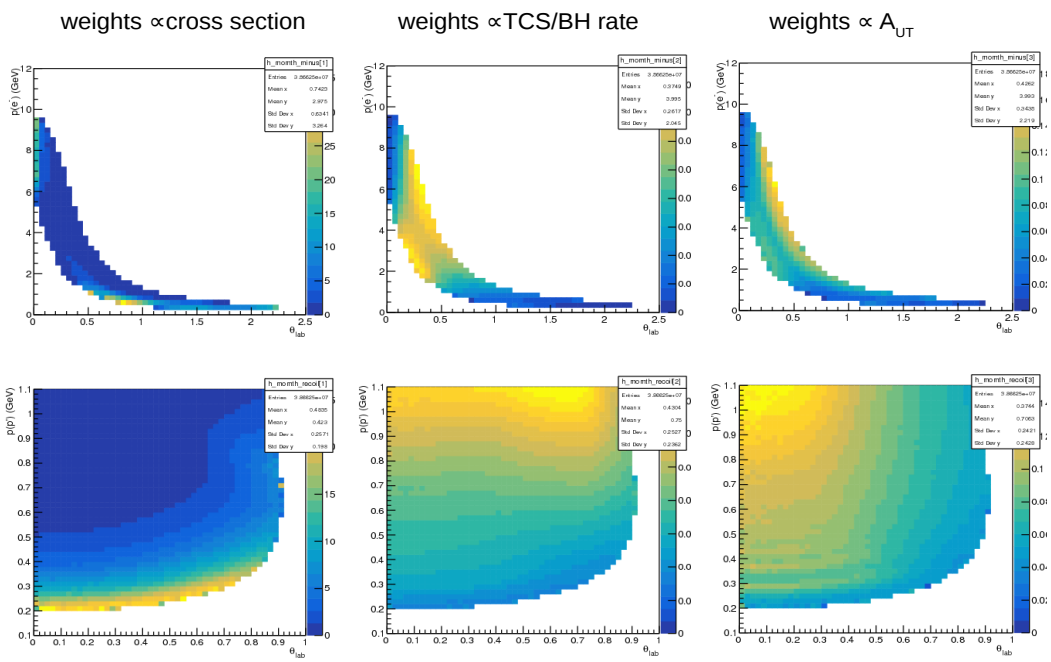

Figure 33: Distribution of momentum versus θ_{lab} for the scattered electron (top row) and the recoil proton (bottom row), weighted by factors proportionnal to the unpolarized cross section (left column), the TCS/BH rate (central column) and the size of the transverse target spin asymmetry (right column).

5 Experimental projections

In this section we describe kinematics, acceptances, analysis methods and projected uncertainties of the proposed experiment. We propose to study photoproduction of lepton pairs, $\gamma p \to l^+ l^- p'$, in a wide range of kinematics. The analysis will use the photoproduction reaction:

$$\gamma p \to e^+ e^- p' \tag{15}$$

where the incoming photon (γ) is real and the final photon has a high timelike virtuality and decays into a lepton pair. In Eq. (15), e^+e^- is the produced lepton pair, and p' is the recoil proton. The final state contains two leptons and a proton, which will provide a coincidence trigger. To suppress background from two-pion photoproduction, the trigger has to contain the two leptons energy cut, at least on the level of 300 MeV. The exclusivity of the reaction is ensured by detecting all final-state particles, e^+e^-p and cutting on the missing-particle kinematics.

This experiment will use 11 GeV energy electron beam incident on 10% radiator to produce high intensity real photons (see Section 3.2). Highly colimated photons will interact with transversely polarized protons (solid ammonia NH_3) yielding luminosities up to $L = 10^{35}$ cm^{-2} sec^{-1}. The detectors will allow for detecting the lepton pair and recoil proton in coincidence. A pair of electromagnetic NPS-type calorimeters will be used for detection of leptons, determination of their energies, and for e/π separation. A pair of recoil detectors will be used to detect protons. These detectors will be combined Hall C basic electronics and DAQ. The experimental setup is shown in Fig. 14. We assume that the NPS-type calorimeters and recoil hodoscope systems will be positioned at angles of from 6° to 21.7° and from -6° to -21.7° up and down relative to beamline, covering $\pm 17°$ in horizontal plane. The proposed design characteristics of the detectors are presented in Table 2.

5.1 Acceptance

The generated lepton and proton tracks were traced through the magnetic field of the target, then scattering chamber window up to the detectors at 1.5 m distance from target. As target field is oriented sideways relative to the beam direction, the tracks are deflected up and down. The track bending happens close to the target, for the field being localized within ~15 cm space at target. The fringe fields do not affect significantly tracks. The high momentum electrons deflect by only $\sim 2°$. While for protons, with momenta from 0.3 to 1.5 GeV/c the bending angle is $\sim 15° - 20°$, typically, and may reach $75°$.

The angular acceptance is limited by the magnet poles and the closely matching to them chamber window: $\pm 17°$ horizontally and $\pm 21.7°$ vertically. The beam pipe downstream the target chamber poses small angle limit of $\pm 6°$. Hence positions and sizes of the lepton and proton detectors, and the tracker as well are chosen to match outgoing track directions (see Sections 3.1, 3.5, 3.4). We display Fig. 34 the t-distribution of accepted events applying a tagging of the two leptons only (blue curve), and applying in addition a tagging of the proton (red curve). The ratio of the curves (bottom panel) corresponds to the impact on the acceptance of the proton tagging.

5.2 Counting rates and projection of the observables

We applied the following phase space and analysis cuts:

- 7.5 < E_γ < 11 GeV (from correlations, we obtain .1 < ξ < .45),

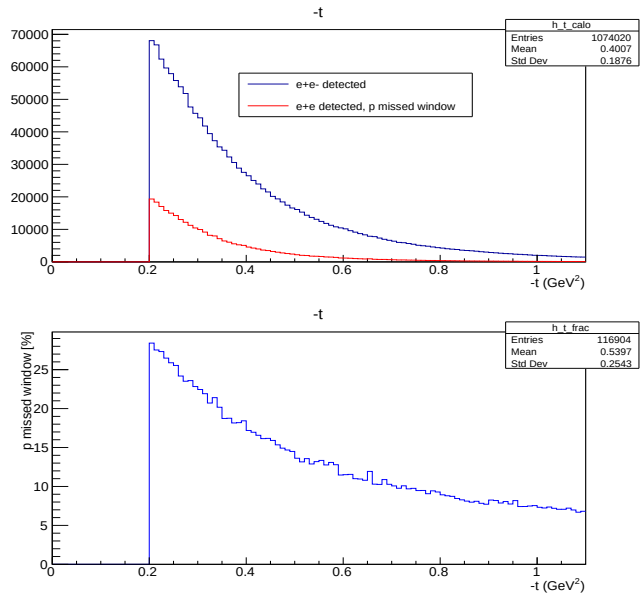

Figure 34: The t-distribution of lepton tagged events (top panel, blue curve) and lepton+proton tagged events (top panel, red curve), and the ratio of these two curves (bottom panel). A cut at -t=0.2 GeV^2 is applied for the purpose of these figures.

- 4 < Q'^{2} < 9 GeV^2,
- 0.04 < -t < 1.04,
- 40° < θ < 140θ in addition to the cut $\theta_{min,max}$ as explicited in section **??**,
- 0° < ϕ < 360°,
- 0° < ϕ_S < 360°,
- 6°<$\theta_{lab}(e^{\pm})$<120°,
- p(p) > 0.1 GeV, p(e$^+$ or e$^-$) > 0.2 GeV,
- tagging of the 2 leptons and the proton.

We defined bins in t, ξ and Q'^2 as presented Fig. 35 for the unpolarized and beam polarized cross sections. For each of these bins, we use 16 bins in ϕ, with additional 16 bin in ϕ_S for transversely target polarized dependent cross sections. We integrated over θ. We display Fig. 36 a projection of the counting rates for the unpolarized cross section, after applying all cuts and acceptance. We display Fig. 37 the beam spin asymmetries with the expected statistic uncertainties. Fig. 38 presents the A_{Ux} and A_{Uy} asymmetries using the same binning (uncertainties are not displayed because the figure will be rebinned). For the selected bin 0.17 < -t < 0.25 GeV^2 and 0.13 < ξ < 0.16, we display the transverse target spin asymmetries as a function of ϕ in ϕ_S bins. Each set of 2 orthogonal transverse spin asymmetry (first row versus second row) provides independent information and will be fitted simultenaously to extract the CFFs.

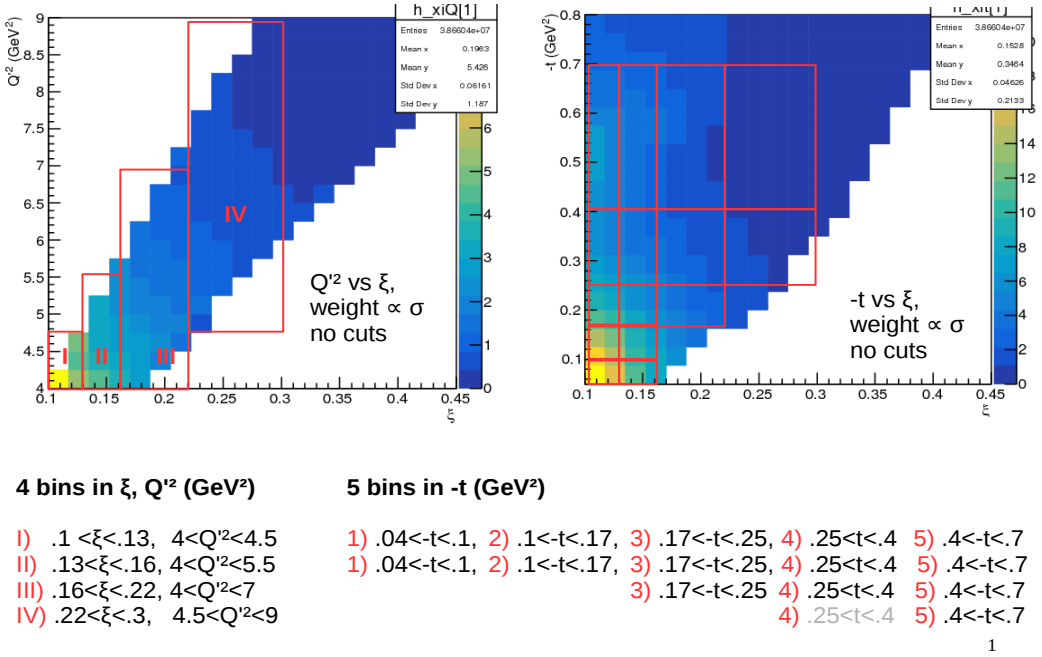

4 bins in ξ, Q'² (GeV²)

I) .1 <ξ<.13, 4<Q'²<4.5
II) .13<ξ<.16, 4<Q'²<5.5
III) .16<ξ<.22, 4<Q'²<7
IV) .22<ξ<.3, 4.5<Q'²<9

5 bins in -t (GeV²)

1) .04<-t<.1, 2) .1<-t<.17, 3) .17<-t<.25, 4) .25<t<.4 5) .4<-t<.7
1) .04<-t<.1, 2) .1<-t<.17, 3) .17<-t<.25, 4) .25<t<.4 5) .4<-t<.7
3) .17<-t<.25 4) .25<t<.4 5) .4<-t<.7
4) .25<t<.4 5) .4<-t<.7

1

Figure 35: Phase space binning for the TCS+BH analysis.

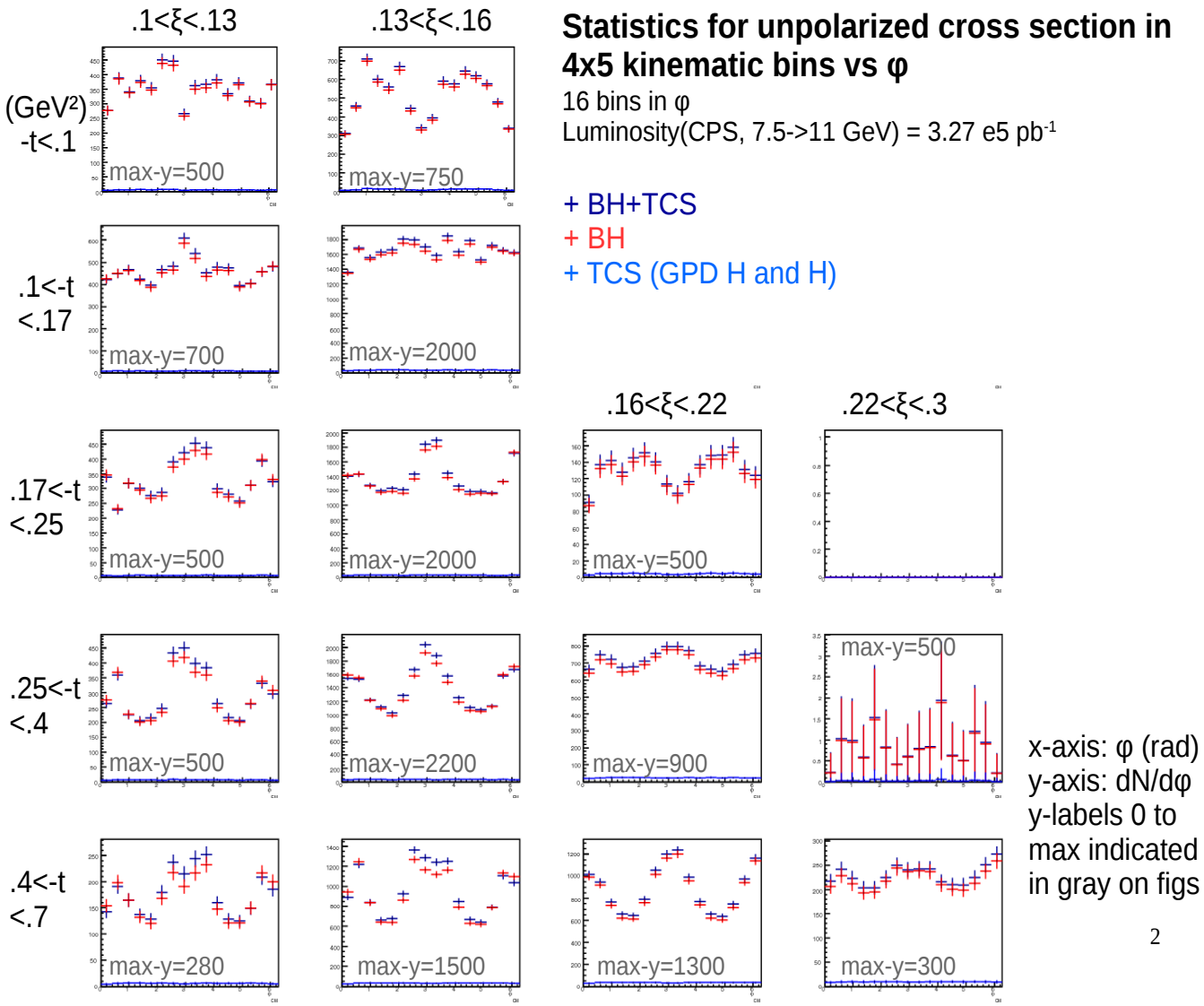

Figure 36: Projection of number of events in each bin as a function of 16 bins in ϕ.

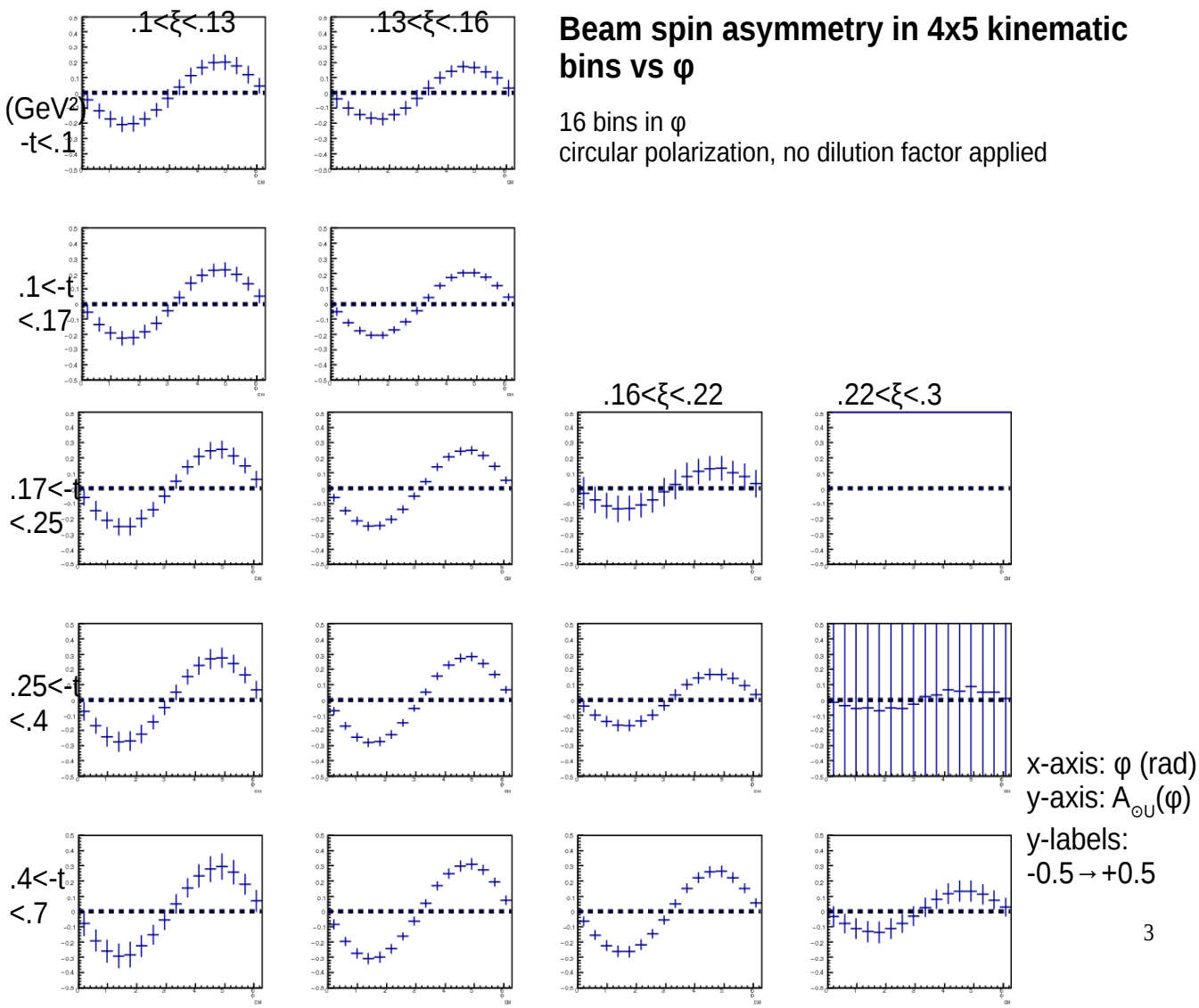

Figure 37: Projection of the single circularly polarized beam spin asymmetries in each bin as a function of 16 bins in ϕ.

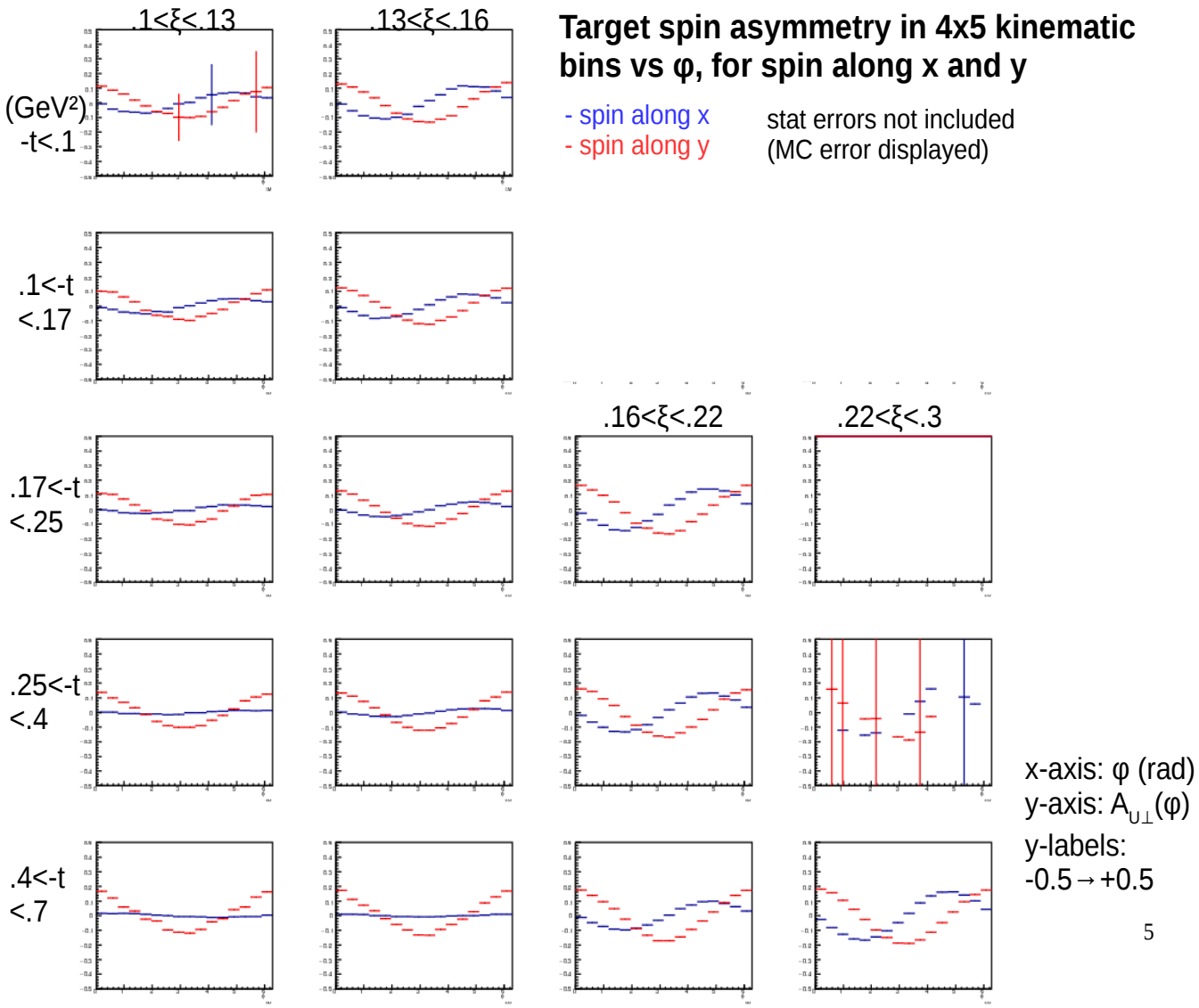

Figure 38: Projection of the single transversely polarized target spin asymmetries at fix ϕ_S, i.e. A_{Ux} (blue) and A_{Uy} (red), in each bin as a function of 16 bins in ϕ.

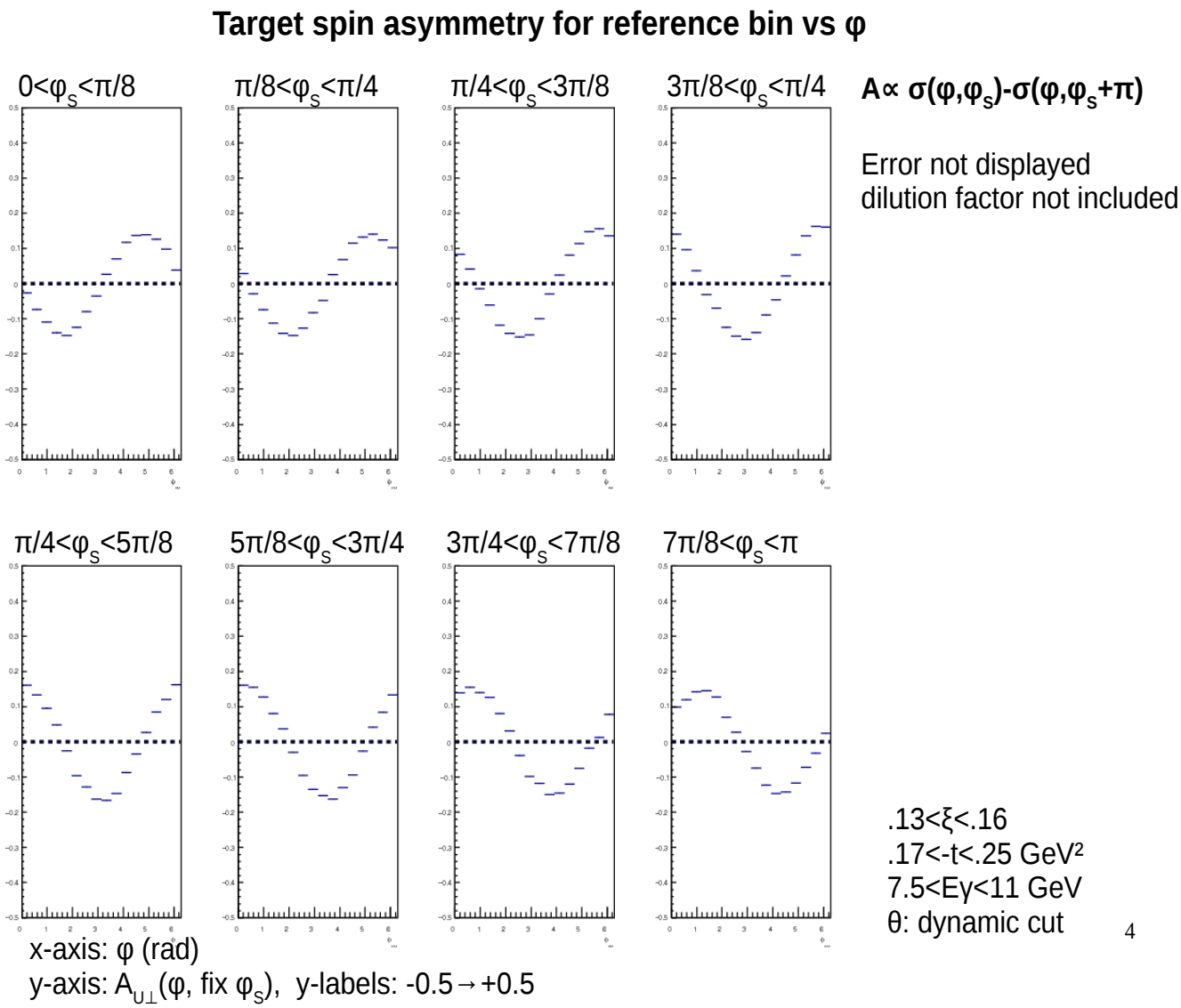

Figure 39: Projection of the single transversely polarized target spin asymmetries in bins of ϕ_S, as a function of 16 bins in ϕ.

6 Conclusion

We propose to the measure TCS+BH transversely polarized target single spin asymmetries, the circularly beam polarized spin asymmetry and the unpolarized cross section. This measurement will held at the Jefferson Laboratory Hall C experimental facility, using a real photon source (Compact Photon Source, CPS), electromagnetic calorimeters as for the Neutral Particle Spectrometer (NPS), and using a transversely polarized target (NH_3 UVa target). The main physics goals of this experiment are:

- Demonstration of GPDs universality by comparing GPDs measured from a spacelike process (DVCS) and a timelike process (TCS, this experiment). The expected level of precision of the universality proof compared to other approved experiments [**?**, **?**] is one order of magnitude better on GPD H, which will allow for discrimination between scenarii of universal or non universal GPDs, and address the milestone of demonstrating QCD structure function universality.

- Extraction of the CFF $\Im E$ of the proton at the same level as achievable from DVCS experiments. This result will allow for constraining quark angular momenta and contribute to the understanding of the nucleon's partonic spin structure.

- Complementarity with DVCS measurement and possibility of combined CFF extraction from TCS and DVCS independently for comparisons, and simultenaoulsy, with new independent information from TCS in order to constrain all protons quark CFF at the same time. It allow for constraining both real and imaginary part of all CFFs simultenaously and bring strong constrain to GPD models. Imaginary part of CFFs can be constrained at a percent level.

We will take advantage of the development of the approved NPS project []. The major hardware development that are required are:

- A second electromagnetic calorimeter similar as the NPS one,

- A scintillator hodoscope based recoil proton detector.

We anticipate a need of 30 days of beam, with a photon luminosity of 10^{35} photons/cm^2/s, which represent 5.85e5 pb$^-1$ integrated luminosity in total for 5.5 to 11 GeV real photons. in order to achieve the presented experimental uncertainties.

7 APPENDIX A: Details about CFF fitting method

7.1 Pseudo-data and methods

All the distributions we generated and used for extracting the CFFs are shown on Fig. 40 (DVCS+BH) and 41 (TCS+BH). Rather than directly fitting the CFF, we extract coefficients of the generated CFFs values from these observables. The coefficients are set to 1 when the generated value is recovered. We limit the variation of all the coefficients during the minimization procedure to stay in a range of $[-5, +5]$, in order to force underconstrained fits to converge. The impact of limitating the variation of the coefficients on uncertainties and on correlation between the extracted CFFs is discussed in [17]. As shown on Fig. 42, the result of the fit (mean value) has a dependence on the starting point and fluctuate around the generated value. However, the $\pm 1\sigma$ limits of the result are stable. To check if CFFs can be extracted from actual data, we also smear the generated cross section points within 1σ of the uncertainties. Similarly, we started the fits from random values of the coefficients. We obtained broader distributions of the results and their limits, with a resolution including the uncertainties on the observables and the correlation between the different CFFs (Fig. 43).

We fitted the results of the fits (CFF value and 1σ errors) by gaus functions. When a given CFF can be extracted from a specific set of observables, we found stable results and allocated the fitted 1σ limits as uncertainties on extracted CFFs. To avoid overcounting the uncertainties on CFFs and in our goal of comparating DVCS and TCS, we used the unsmeared distributions of pseudo-data for this exercise.

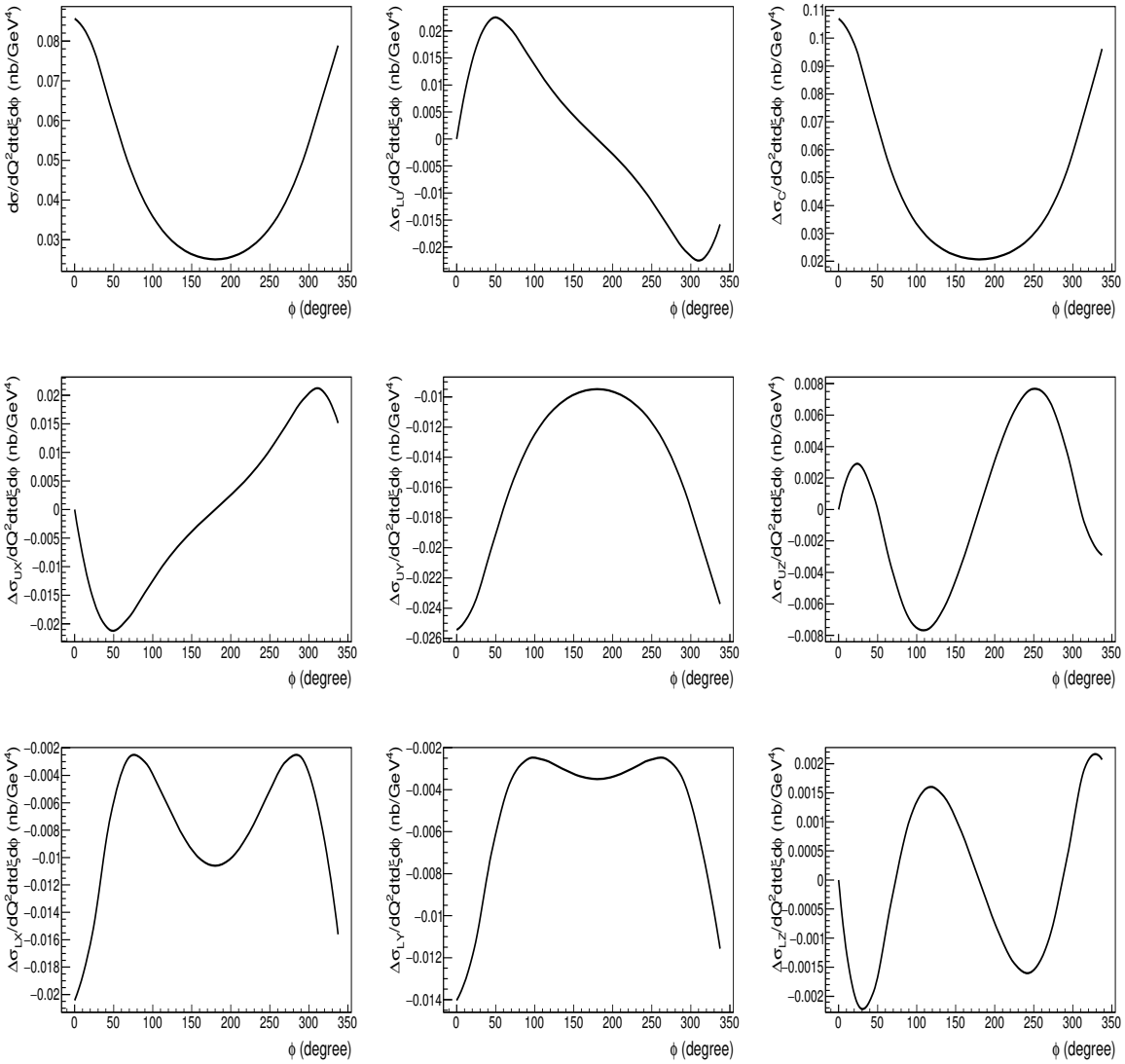

Figure 40: Generated distributions for DVCS+BH process. First row: unpolarized cross section, beam spin cross section difference, beam charge cross section difference. Second row: single target spin cross section differences (target spin along x, y, z). Third row: double spin cross section differences (target spin along x, y, z).

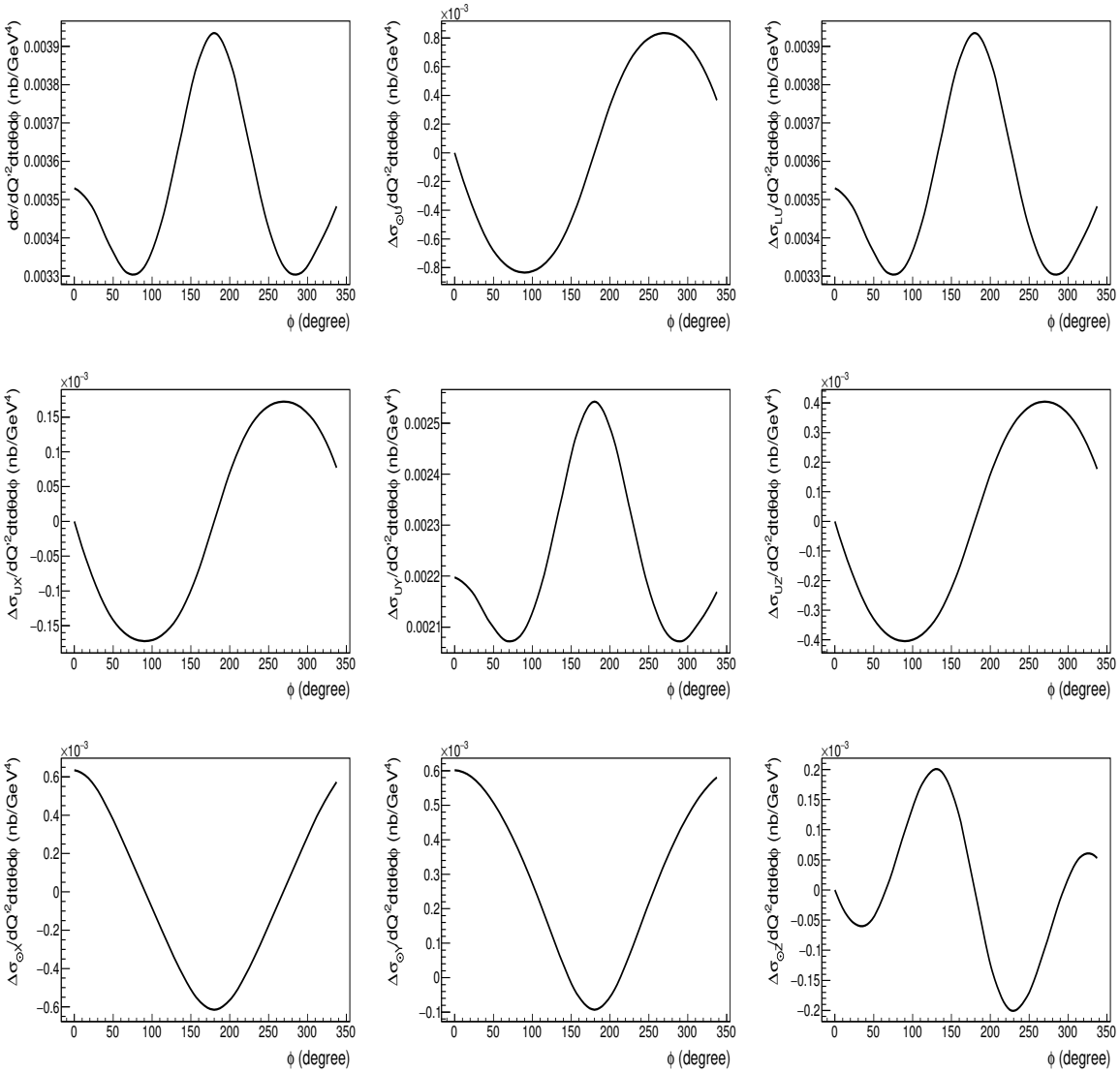

Figure 41: Generated distributions for TCS+BH process. First row: unpolarized cross section, circularly polarized beam spin cross section difference, longitudinaly polarized beam cross section difference. Second row: target polarized cross section differences (target spin along x, y, z). Third row: double beam and target polarized cross section difference (target spin along x, y, z).

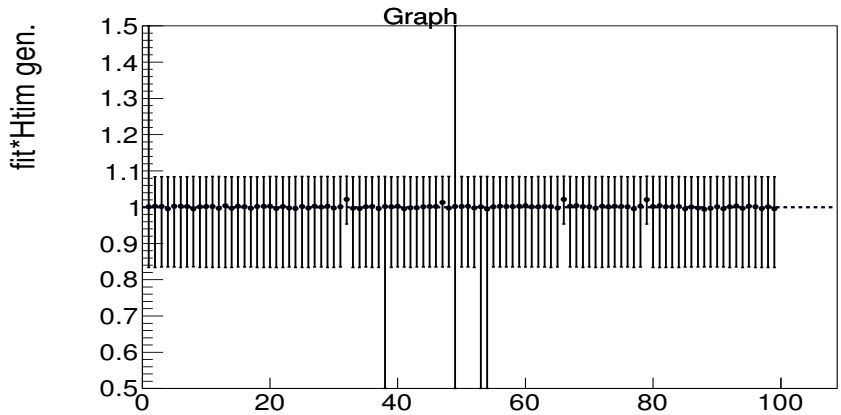

Figure 42: Result for $\Im\tilde{\mathcal{H}}$ of fitting 100 time the same distribution starting from a random value for all CFF coefficients in $[-5, +5]$. We fitted simultenaously DVCS+BH unpolarized cross section, beam spin and longidutinal target single and double polarized cross section differences.

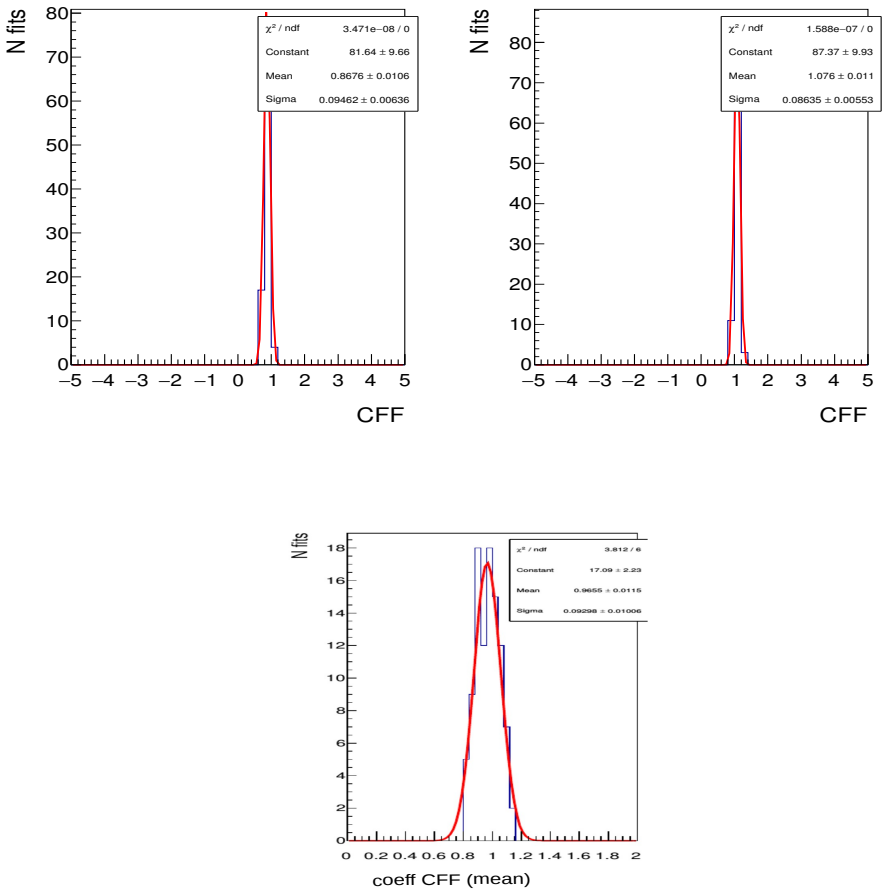

Figure 43: Top: Minimal (left) and maximal (right) limits of $\Im\tilde{\mathcal{H}}$ extracted from fitting 100 times smeared distributions of the same observables, and starting from a random value for all CFF coefficients in $[-5, +5]$. Bottom: fit result (central value) for the same distributions. We fitted simultenaously DVCS+BH unpolarized cross section, beam spin and longidutinal target single and double polarized cross section differences.

References

[1] D. Müller, D. Robaschik, B. Geyer, F.-M. Dittes and J. Hořejši, Fortsch. Phys. **42** (1994) 101

[2] X. D. Ji, Phys. Rev. D **55** (1997) 7114

[3] A. V. Radyushkin, Phys. Rev. D **56** (1997) 5524

[4] Goeke K, Polyakov M V and Vanderhaeghen M 2001 *Prog. Part. Nucl. Phys.* **47** 401

[5] M. Diehl, Phys. Rept. **388** (2003) 41

[6] M. Guidal, H. Moutarde and M. Vanderhaeghen, Rept. Prog. Phys. **76** (2013) 066202

[7] Vanderhaeghen M, Guichon P A M and Guidal M 1998 *Phys. Rev. Lett.* **80** 5064

[8] M. Vanderhaeghen, P. A. M. Guichon and M. Guidal, Phys. Rev. D **60** (1999) 094017 doi:10.1103/PhysRevD.60.094017

[9] Guidal M, Polyakov M V, Radyushkin A V and Vanderhaeghen M 2005 *Phys. Rev. D* **72** 054013

[10] A. V. Radyushkin, Phys. Rev. D **59** (1999) 014030

[11] A. V. Radyushkin, Phys. Lett. B **449** (1999) 81

[12] M. Boër, M. Guidal and M. Vanderhaeghen, Eur. Phys. J. A **51** (2015) no.8, 103.

[13] E. R. Berger, M. Diehl and B. Pire, Timelike Compton scattering: exclusive photoproduction of lepton pairs, The European Physical Journal C23 (2002) 675-689

[14] Guidal M 2008 *Eur. Phys. J. A* **37**, 319 [Erratum-ibid. A **40**, 119 (2009)]

[15] A.V. Radyushkin, Phys. Lett. B 380 (1996) 41

[16] A.V. Belitsky, D. Mueller and A. Kirchner, Nucl. Phys. B629 (2002) 323.

[17] M. Boër and M. Guidal, J. Phys. G **42** (2015) no.3, 034023

[18] P. A. M. Guichon and M. Vanderhaeghen, Phys. Rev. Lett. **91** (2003) 142303

[19] E. J. Brash, A. Kozlov, S. Li and G. M. Huber, Phys. Rev. C **65** (2002) 051001

[20] O. Gayou *et al.* [Jefferson Lab Hall A Collaboration], Phys. Rev. Lett. **88** (2002) 092301

[21] JLab experiment E12-12-001: Timelike Compton Scattering and J/ψ photoproduction on the proton in e^+e^- pair production with CLAS12 at 11 GeV,
note = http://www.jlab.org/exp_prog/proposals/12/PR12-12-001.pdf.

[22] M. Kubantsev et al., Performance of the Primex Electromagnetic Calorimeter, arXiv:physics/0609201, 22 Sep. 2006; A. Gasparyan, Performance of PWO crystal Detector for a High Resolution Hybrit Electromagnetic Calorimeter at Jefferson Lab., Proceed. X Int. Conf. Calorimetry in Particle Physics, Perugia, Italy, 29 March-2 April 2004, pp. 109-115.

[23] Measurement of Semi-Inclusive π^0 Production as Validation of Factorization, JLab Experiment E12-13-007, R. Ent, T. Horn, H. Mkrtchyan and V. Tadevosyan spokespersons. Proposal aproved in 2015 by JLab PAC40.

[24] The Charge Form Factor of the Neutron, JLab experiment E93-026, D. Day spokesperson.

[25] Precision Measurement of the Nucleon Spin Structure Functions in the Region of the Nucleon Resonances, JLab experiment E01-006, O. Rondon Aramayo spokesperson.

[26] Spin Asummetries on the Nucleon Experiment:SANE, JLab experiment E07-003, S. Choi, Z.E. Meziani, O. Rondon-Aramayo spokespersons.

[27] GeN Technical Note.

[28] D. Crabb and D. Day, *"The Virginia/Basel/SLAC polarized target: operation and performance during experiment E143 at SLAC"*. Nucl. Inst. Meth. **A**356, 9-19 (1995).

[29] H. Zhu, *"A Measurement of the Neutron Electric Form Factor in $\vec{D}(\vec{e}, e'n)p$ Quasi-elastic Scattering at $Q^2_= 0.5\,(GeV/c)^2$"*. Ph.D. Dissertation, University of Virginia, Charlottesville (2000).

[30] UVa target group web page: *http://twist.phys.virginia.edu/documents.html*.

[31] Event generator for TCS from R. Paremuzyan.

[32] Proceedings from High Intensity Photon Sources Workshop (CUA, 2/6–2/7 2017), https://arxiv.org/pdf/1704.00816.pdf

[33] Polarization Observables in Wide-Angle Compton Scattering at large s, t, and u. G. Niculescu,B. Wojtsekhowski, D. Day, D. Keller, J. Zhang,D.J. Hamilton co-spokespersons. Proposal C12-17-008 conditionally approved by JLab PAC45 in 2017.

[34] M. Boër, DEEPGen: polarized BH+TCS event generator, `https://hallaweb.jlab.org/wiki/index.php/DDVCS_and_TCS_event_generator` (2015).